nature communications

Article

https://doi.org/10.1038/s41467-026-73979-0

A stretch-responsive fibroblast program promotes epidermal stem cell self-renewal during skin expansion

Received: 24 February 2025

Accepted: 27 May 2026

Published online: 12 June 2026

Check for updates

Caroline Aguilera Stewart[1,9], Ceyhun Alar[2,3,9], Gaia Andrea Gozza[4,5,9], Leslie Bargsted[1], Ioanna Kaklamanou[1], Maria Pia Polito[4,5], Giulia Bergamini[4,5], Lorenzo Tagliazucchi[5,8], Andrea Alessandrini[6,7], Maria Paola Costi[5], Elena Enzo[4,5] ✉, Alejandro Sifrim[2,3] ✉ & Mariaceleste Aragona[1] ✉

Stretch-mediated tissue expansion is commonly used to grow extra skin for reconstructive surgeries. To ensure harmonious growth, the two main skin compartments, the epidermis and the dermis, must both expand in a coordinated manner. How fibroblasts respond to stretch-mediated tissue expansion in supporting keratinocyte proliferation remains unclear. Here we map the fibroblast transcriptional response to stretching in vivo and demonstrate that stretching forces fibroblasts to exit their quiescent state and restart proliferation. Concurrently, fibroblasts reduce collagen production and upregulate extracellular matrix remodelling factors, adopting a more embryonic-like program. Because embryonic fibroblasts are widely used as feeder layers to support the expansion of epidermal stem cells for clinical application, we leveraged this model to show that a low collagen state enhances epidermal stem cell self-renewal, thereby coordinating epidermal and dermal responses during skin expansion. These findings provide valuable insights to guide the design of in vivo stretch-mediated tissue expansion protocols and the production of in vitro skin grafts for clinical application.

The skin serves as the body's outermost layer, playing a crucial role in protecting against external threats[1]. Within epithelial tissues, mechanical forces are continuously present during homoeostasis and wound healing, ensuring the restoration of tissue integrity and the preservation of its intrinsic functions[2–6]. Mechanotransduction converts mechanical stimuli into biochemical signals and gene transcription, thereby influencing not only tissue morphology but also cell behaviour[7,8]. To establish and maintain functional organs, the tissue response to these mechanical forces must be precisely coordinated across different compartments[9].

Stretch-mediated tissue expansion is a common plastic surgery technique that promotes the growth of extra skin that can then be transplanted for repairing birth defects, scars, or creating space for permanent implants in breast reconstruction following mastectomy[10–12]. Due to its capacity to adapt and respond to external physical stimuli, the skin is an excellent model to study cellular interactions and compartment coordination under mechanical forces[1,13,14]. Few animal models of in vivo skin expansion have been described[15–20]. A model was established in mice, using self-inflating hydrogel

[1]Novo Nordisk Foundation Center for Stem Cell Medicine (reNEW), Department of Biomedical Sciences (BMI), University of Copenhagen, Copenhagen, Denmark. [2]KU Leuven Institute for Single Cell Omics (LISCO), University of Leuven, KU Leuven, Leuven, Belgium. [3]Department of Human Genetics, University of Leuven, KU Leuven, Leuven, Belgium. [4]Centre for Regenerative Medicine "Stefano Ferrari", University of Modena and Reggio Emilia, Modena, Italy. [5]Department of Life Sciences, University of Modena and Reggio Emilia, Modena, Italy. [6]Department of Physics, Informatics and Mathematics, University of Modena and Reggio Emilia, Modena, Italy. [7]CNR-Nanoscience Institute-S3, Modena, Italy. [8]Present address: University of Parma, Food and Drug Department, Parma, Italy. [9]These authors contributed equally: Caroline Aguilera Stewart, Ceyhun Alar, Gaia Andrea Gozza. ✉e-mail: elena.enzo@unimore.it; alejandro.sifrim@kuleuven.be; mariaceleste.aragona@sund.ku.dk

expanders, to mimic the expansion process in humans[15]. This model was used to study the effects of stretching on the epidermis, revealing that epidermal stem cells' fate decisions were transiently biased towards self-renewal[15]. However, the response of fibroblasts, the main cellular component of the dermis, to stretching has not been studied to date[21]. Human epidermis can also be expanded in vitro under defined conditions that require fibroblasts to sustain keratinocytes' self-renewal potential[22]. However, how fibroblast hallmarks drive keratinocyte expansion in vitro is not fully understood. In particular, how fibroblasts and keratinocytes coordinate their responses to expansion, and which fibroblast-specific traits provide signals that promote epidermal stem cell self-renewal, remains unknown.

Here, we investigate how dermal fibroblasts respond to stretch and how this response influences epidermal stem cell behaviour. Using an in vivo model of stretch-mediated tissue expansion and complementary in vitro approaches, we show that stretch induces a proliferative, matrix-remodelling, embryonic-like fibroblast programme characterised by reduced collagen deposition, which promotes epidermal stem cell self-renewal.

Results

A transcriptomic atlas of stretch-mediated skin expansion

To study the effect of stretch-mediated skin expansion more broadly on the skin, we performed single-cell RNA sequencing (scRNA-seq) in control (CTRL) and expansion (EXP), using the previously described mouse model[15]. All mice underwent surgery, whilst the CTRL mice did not have an expander inserted (Fig. 1a). Live skin cells were isolated by fluorescence-activated cell sorting (FACS) (Supplementary Fig. 1a). We profiled living cells at day 1 (D1), when the maximal stretch is reached, and at day 2 (D2) and day 4 (D4) when the epidermal stem cells are biased towards self-renewal[15] (Fig. 1a–c and Supplementary Fig. 1b–g, Supplementary Tables 1, 2 and Supplementary Data 1). In the entire atlas ($n = 32$ animals, $n = 22.412$ CTRL cells and $n = 13.904$ EXP cells) we uncovered all the different cell types constituting the mouse back skin[23–25] (Fig. 1b, c, Supplementary Fig. 1c–g, Supplementary Tables 1, 2 and Supplementary Data 1). The keratinocyte and monocyte clusters contain proportionally more EXP cells, consistent with previous reports on epidermal expansion and inflammatory cell recruitment[15,19,20]. These proportions change over time: both keratinocytes and monocytes increase in number in the EXPD2 and EXPD4 samples (Supplementary Fig. 1e, g). In contrast, the fibroblast cluster contains a consistently higher proportion of CTRL cells across all timepoints (Supplementary Fig. 1b, e, g and Supplementary Data 2). While in previous work we described the active role of keratinocytes[15], and how in this context, inflammation does not play a significant role in tissue expansion[15], here we investigate the role of fibroblasts in more depth.

scRNA-seq of fibroblasts

Fibroblasts and other stromal cells are the most important cell types in the dermis, providing structural support and modulating different biological processes[21,26,27]. However, their role in skin expansion and their functional interaction with keratinocytes in this context remain not fully understood. In total, there were 15.419 fibroblast and stromal cells (also referred to as fibroblast-like cells in the text) in our dataset (Fig. 1d, and Supplementary Fig. 1b–g). Using graph-based clustering, we identified different subpopulations based on marker gene expression as described in previous studies[24,28,29]. We distinguished eight subclusters of fibroblasts (FIB1-8), as well as two dermal papilla (DP1-2) and one dermal sheath subcluster (DS) (Fig. 1d and Supplementary Data 3). The proportions of the different fibroblast subtypes changed during expansion (Fig. 1e, Supplementary Fig. 2a–f and Supplementary Data 4), with a pronounced enrichment of FIB4 and FIB6 clusters specifically. Samples from the CTRL and EXP conditions were well distributed between the fibroblast subclusters (Supplementary Fig. 2a–c). However, a dynamic shift in distribution of these subclusters was observed over time in EXP (Supplementary Fig. 2e, f), and this pattern was overall consistent across samples (Supplementary Fig. 2g, h). Subclusters FIB1-3 were more transcriptionally similar than the other fibroblast subpopulations, FIB5-8 (Fig. 1f). The FIB4 subpopulation, whilst expressing many similar genes to FIB1-3, also shows higher expression of Podoplanin (*Pdpn*), Tenascin C (*Tnc*) and Tissue Inhibitor of Metalloproteinase 1 (*Timp1*) (Fig. 1f). The transcriptional similarity of FIB4 to FIB1-3 subclusters may indicate that FIB4 is a cell state rather than a new fibroblast subtype, as suggested by pseudotime analysis (Supplementary Fig. 3a–c), becoming more prominent during expansion (Supplementary Fig. 2d–h and Supplementary Data 4). The subcluster FIB8 ($n = 350$ cells) has overall lower counts and higher ribosomal gene expression, and we could not identify unique marker genes for this population. Therefore, we excluded it from further analyses.

Spatial mapping of fibroblast subpopulations

As we are interested in fibroblast interactions with keratinocytes, we performed spatial transcriptomics on four CTRL skin samples to determine whether the fibroblast subclusters identified in the scRNA-seq analysis inhabit spatially distinct niches and which clusters are present in the upper dermis closer to the keratinocytes. We used the 10x Genomics Xenium platform to run a panel of 95 custom genes, selected by a deep learning model to maximally preserve the transcriptional information of our scRNA-seq dataset, together with 379 genes from the predesigned Xenium mouse tissue atlas. Cells in the spatial dataset were annotated based on the gene expression signatures we found in our scRNA-seq dataset (Fig. 1d–f and Supplementary Fig. 4a–e). We concluded that subpopulations FIB1-4 were mostly located in the upper dermis, and subclusters 5–7 were more enriched in the lower regions of the skin (Fig. 2a–c and Supplementary Fig. 4f, g). We identified *Pdpn* as a marker enriched in the upper dermis (Fig. 2d and Supplementary Fig. 4h), whereas expression of *Gpx3* and *Mfap5*, as expected[24], was mostly restricted to the lower dermis (Fig. 2e,f and Supplementary Fig. 4i, j). The platelet-derived growth factor receptor alpha (*Pdgfrα*), which is commonly used as a general marker of dermal fibroblasts[30] was broadly expressed in both upper and lower dermis (Supplementary Fig. 4k). We thus established that in the mouse dorsal skin, the transcriptional heterogeneity reflects at least two spatially distinct anatomical regions of the upper and lower dermis.

Stretching induces a transcriptional response in fibroblasts

To dissect the response of fibroblasts to stretching, we decided to look further into the gene expression profiles of fibroblasts in our scRNA-seq dataset, focusing in particular on the upper dermis. In the expanded condition, taking into account all fibroblast subclusters, we observed upregulation of extracellular matrix (ECM) remodelling glycoprotein genes like *Pdpn*, *Tnc* and *Timp1* as well as genes that have been previously associated with an embryonic-like and regenerative fibroblast signature (*Crabp1* and *Mmp13*, also known as collagenase-3)[28,31,32], and *Pdgfrα* (Fig. 3a and Supplementary Data 5). The transcriptional changes observed were consistent across mice (Supplementary Fig. 5a–c). Interestingly, the expression of ECM remodelling genes *Pdpn*, *Tnc*, and *Timp1* was enriched in the FIB4 subcluster, whose location is restricted to the upper dermis according to our spatial mapping (Fig. 2a, c). To validate these results by qPCR, we enriched for fibroblasts via Fluorescence-activated cell sorting (FACS), first through exclusion of vasculature, hematopoietic, melanocyte and epithelial cells (cells expressing CD31, CD45, CD117 and EPCAM, respectively) and then inclusion of CD34+ and PDGFRA+ cells[30], selecting for double positive CD34+ and PDGFRA+ cells allowed us to collect most upper dermal fibroblasts whilst excluding hair follicle-related fibroblasts, such as DP fibroblasts (Supplementary Fig. 5d–f)[30] a location that is

https://doi.org/10.1038/s41467-026-73979-0

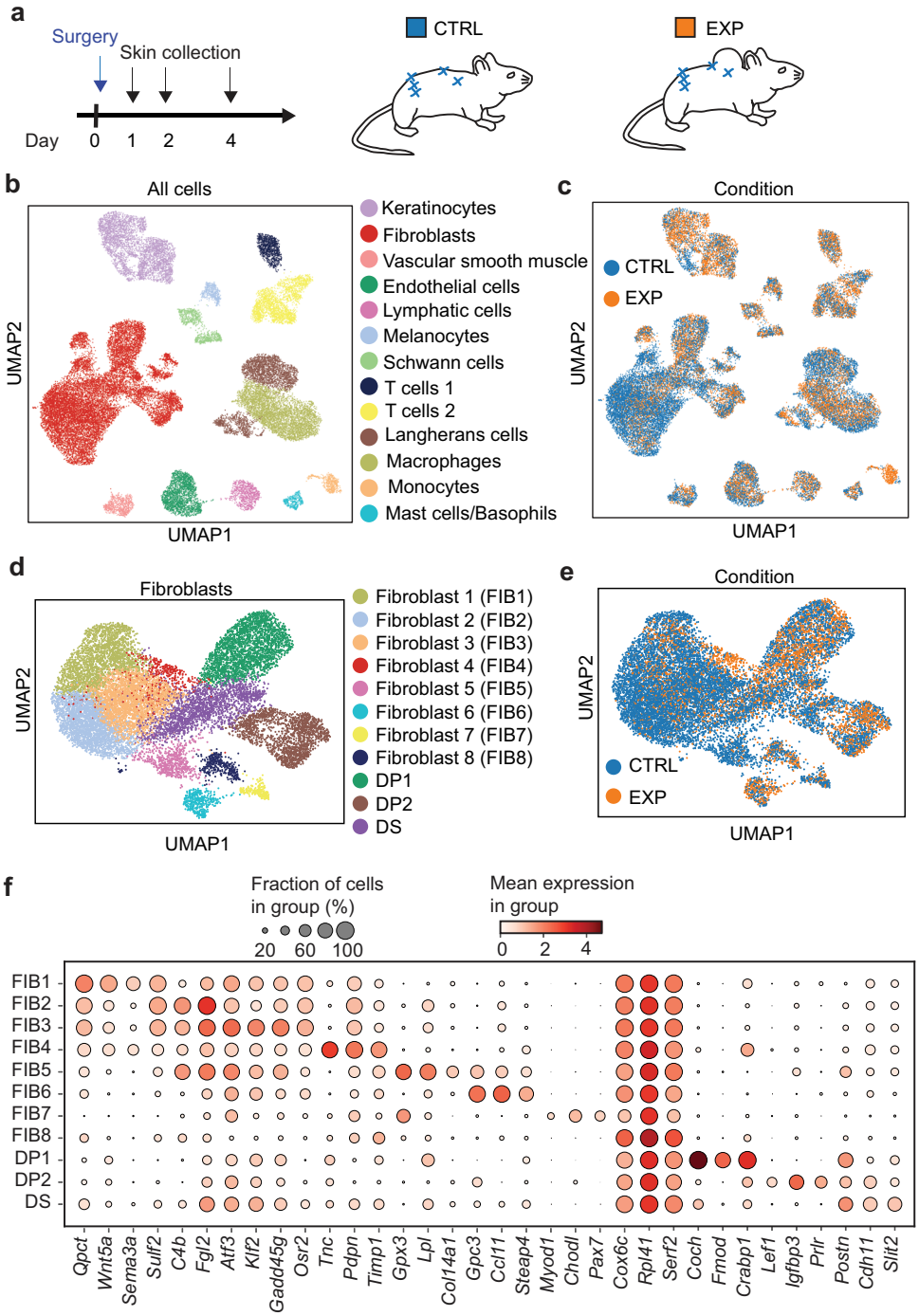

Fig. 1 | Single-cell RNA sequencing of stretch-mediated skin expansion. **a** Schematic of the experimental procedure and stretch-mediated skin expansion mouse model. **b** UMAP plot of the clustering analysis of scRNA-seq data of CTRL (22412 cells, number of mice: D1 = 4, D2 = 7, D4 = 4) and EXP (13904 cells, number of mice: D1 = 4, D2 = 7, D4 = 4) samples. **c** UMAP plot of the distribution of CTRL and EXP cells within clusters shown in (**b**). **d** UMAP plot of the sub-clustering analysis of CTRL (11634 cells) and EXP (3785 cells) fibroblast and fibroblast-like cells. **e** UMAP plot of the distribution of CTRL and EXP cells within subclusters shown in (**d**). **f** Marker gene expression for each of the subclusters shown in (**d**).

confirmed by immunostaining experiments (Supplementary Fig. 5g, h). Downregulation of *Cd34* upon expansion was observed at the transcriptomic level in the scRNA-seq (Fig. 3a and Supplementary Data 5) and via qPCR (Supplementary Fig. 5e) and confirmed at the protein level via flow cytometry (Supplementary Fig. 5f) and immunostaining (Supplementary Fig. 5i, j). Previously, *Cd34* has been described as downregulated in neonatal fibroblasts compared to adult fibroblasts[33]. We confirmed the upregulation of *Pdpn*, *Tnc*, *Timp1* and *Mmp13* via qPCR (Fig. 3b–e). The increased expression of *Pdpn* and *Tnc* during expansion was also confirmed by immunostaining at D2 and D4 (Fig. 3f–i and Supplementary Fig. 5k). The matrix metalloproteinases (MMPs) and the tissue inhibitors of metalloproteinases (TIMPs) are both required in dynamic contexts of active ECM remodelling[34]. The overexpression of these genes, along with the glycoproteins *Pdpn* and *Tnc*, suggests that the ECM composition changes during tissue expansion, becoming more compliant and viscoelastic[35–37]. It has also been previously demonstrated that *Pdpn* and *Tnc* are expressed during development, but their expression becomes limited in healthy adult

https://doi.org/10.1038/s41467-026-73979-0

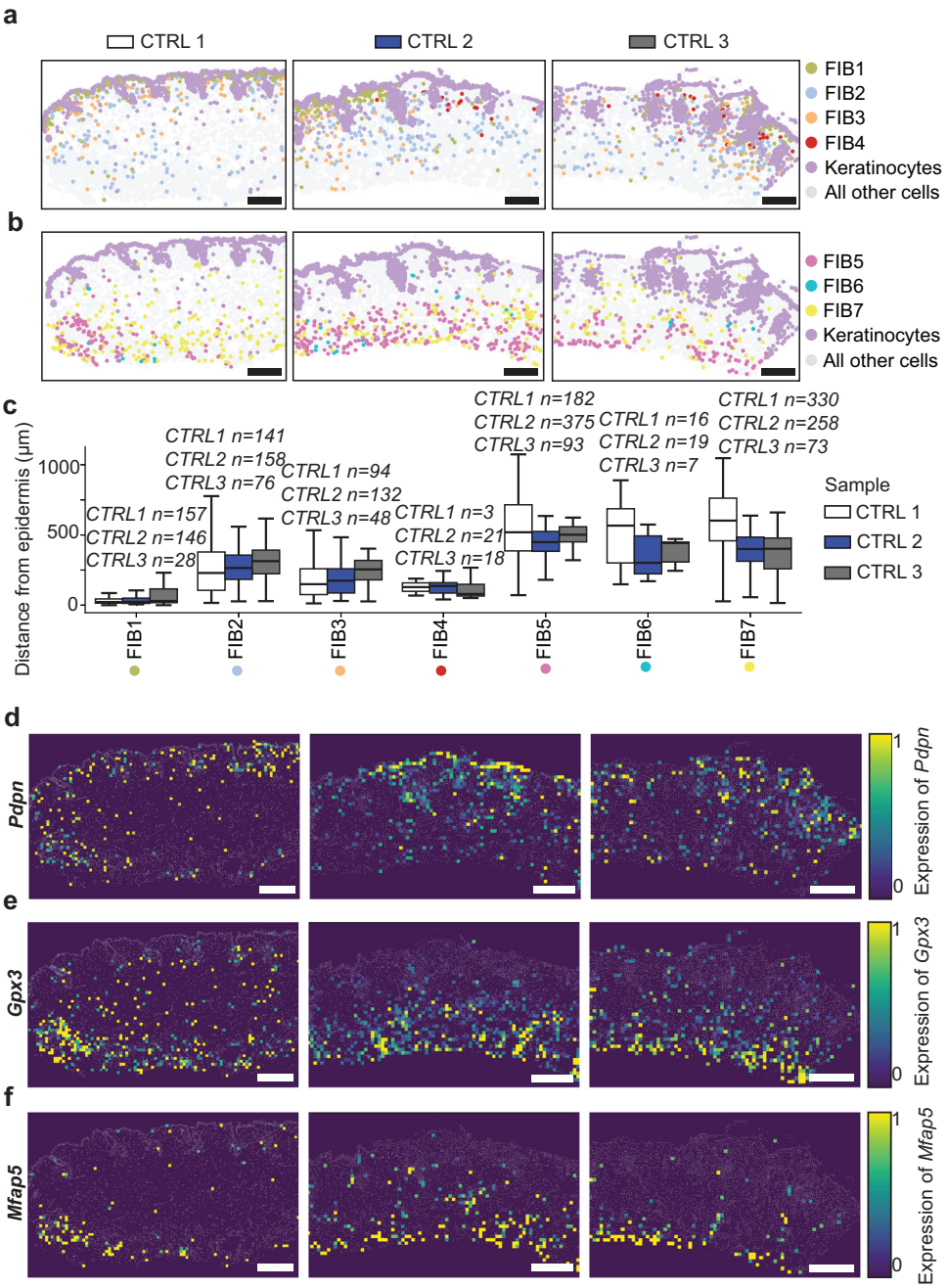

Fig. 2 | Spatial mapping of fibroblast subpopulations. a Representative image of the spatial distribution of FIB1-4 subpopulations in D2 CTRL skin ($n = 3$ section per mouse). Keratinocytes are shown in purple. Bin size = 20 µm. **b** Representative image of the spatial distribution of FIB5-7 subpopulations in D2 CTRL skin ($n = 3$ sections per mouse). Keratinocytes are shown in purple. Bin size = 20 µm. **c** – Fibroblast distance from the epidermis per sample and fibroblast subtype. Boxes show median and interquartile range with 1.5 x IQR whiskers. N = number of cells per cluster is indicated. **d**–**f** Representative images of the spatial density plots showing relative expression of *Pdpn*, *Gpx3* and *Mfap5* transcripts. Nuclei are shown in grey. Scale normalised per gene transcript. Bin size = 20 µm. All scale bars = 200 µm. Source Data are provided as Source Data file.

tissues[33,38,39]. Altogether, the upregulation of *Pdpn*, *Tnc*, *Timp1*, and the downregulation of *Cd34* suggest that during expansion, fibroblasts reacquire a signature that is more similar to an earlier developmental and regenerative state. These data also show that fibroblasts respond to stretching by changing their transcriptional landscape quite rapidly.

Fibroblasts spatial reorganisation during skin expansion

Given that we identified transcriptional changes in the fibroblasts in response to stretching, we wanted to understand whether these changes were associated with differences in fibroblasts appearance, especially in the upper dermis. To gain a phenotypic overview of the morphological changes occurring in the fibroblasts during expansion, we traced stromal cells positive for PDGFRA. We used *PdgfraCre-ERT2;Rosa26*^{mTmG} reporter mice to visualise the cell membranes of fibroblasts (Fig. 4a, b and Supplementary Fig. 6a). Using a high dose of induction to study fibroblasts at the population level, we were able to recombine on average 67% of PDGFRA+ cells, as assessed by flow cytometry (Supplementary Fig. 6b, c). Immunofluorescence staining for PDGFRA on *PdgfraCre-ERT2;Rosa26*^{mTmG} sections revealed good overlap between the signal of the immunofluorescence for PDGFRA

https://doi.org/10.1038/s41467-026-73979-0

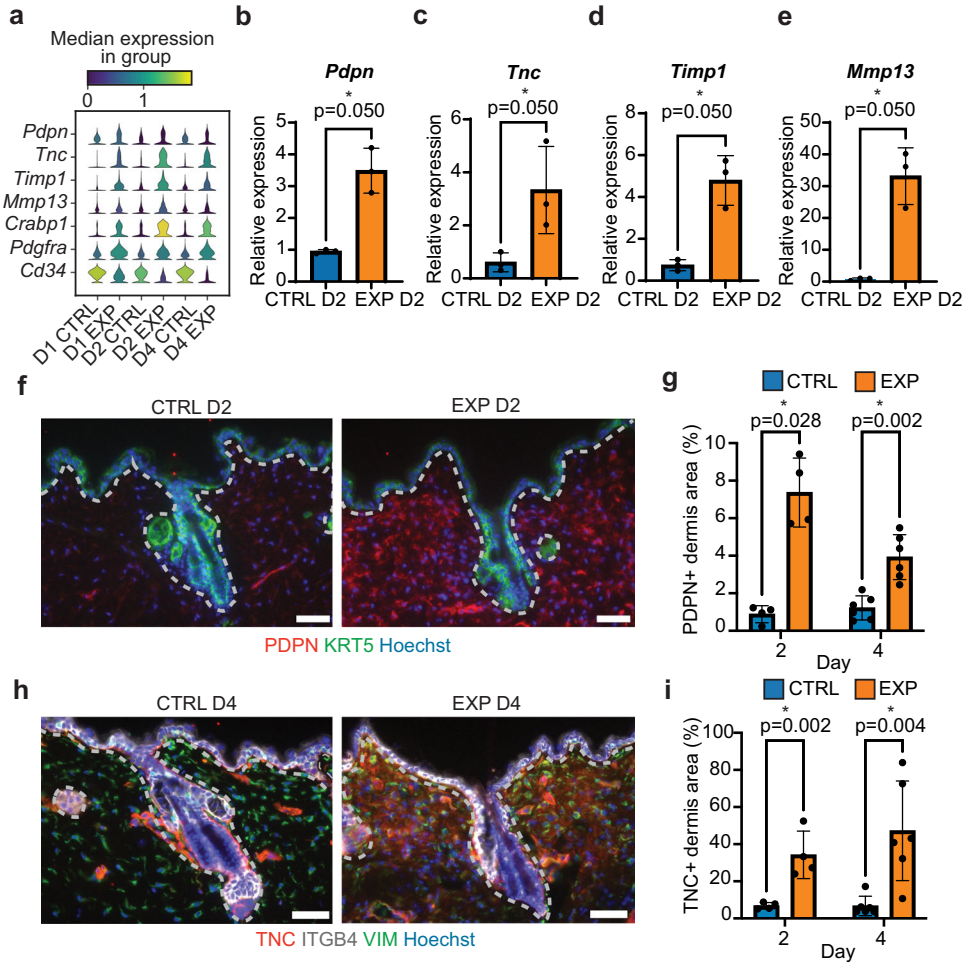

Fig. 3 | Transcriptional changes in fibroblasts upon expansion. a Stacked violin plot of differentially expressed genes (DEG) in fibroblast and fibroblast-like cells from scRNA-seq. **b**–**e** Relative expression of the indicated genes in sorted PDGFRA+ and CD34+ fibroblasts by qPCR at D2. Unpaired one-tailed Mann-Whitney U-tests, $n = 3$ mice per condition. Data are presented as mean +/− SD. **f** Immunofluorescence for PDPN (red), KRT5 (green) and Hoechst (blue) on D2 CTRL and EXP skin. White dotted lines separate the epidermis and hair follicles from the dermis. Only the upper region of the dermis is displayed. **g** Quantification of the PDPN + area in the upper dermis, from (**f**). Unpaired two-tailed Mann-Whitney U-tests, $n = 4$ mice per condition at D2 and $n = 6$ mice per condition at D4, the dots represent means of 3 measurements per mouse. Data are presented as mean +/− SD. **h** Immunofluorescence for TNC (red), ITGB4 (white), VIM (green) and Hoechst (blue) on D4 CTRL and EXP skin. Dotted white lines delimit the epidermis and hair follicles. Only the upper region of the dermis is displayed. **i** Quantification of the TNC+ area in the upper dermis from (**h**). Unpaired two-tailed Mann-Whitney U-tests, $n = 4$ mice per condition at D2 and $n = 6$ mice per condition at D4, averages of 3 measurements per mouse are plotted as dots. Data are presented as mean +/− SD. All scale bars = 50 µm. Source Data are provided as a Source Data file.

and the signal of the green fluorescence protein (GFP) from the recombined endogenous *Pdgfra*-GFP (Supplementary Fig. 6d). We focused on the upper dermis region for subsequent morphological analyses (as defined in Supplementary Fig. 6a) in Fig. 4c–f and Supplementary Fig. 6e–h, unless otherwise stated, as we observe particular molecular changes in fibroblasts located in this area and to try to exclude any potential confounding contributions from fascia progenitors[40,41]. Upon stretching, the surface area of the skin increases, as previously measured[15]. However, rather than a thinner dermis, we observe that the dermis thickness remains unchanged post-expansion (Supplementary Fig. 6e, f), suggesting that new stroma is generated to compensate for the larger area of skin produced. Indeed, the total fibroblast volume in the upper dermis, calculated based on the signal of the *Pdgfra*-GFP, increased at D2 and D4 during expansion (Fig. 4b, c). We also observed changes in the organisation of the *Pdgfra*-GFP signal. To quantify these morphological changes, we took advantage of the ImageJ plugin FracLac that measures the complexity of morphology[42]. At D2 and D4, the *Pdgfra*-GFP signal had a lower fractal dimension score, indicating a less complex arrangement of the labelled cells (Fig. 4d, e). The overall cell density in the dermis was significantly increased at D4 (Fig. 4f), whilst cell death, as assessed by cleaved Caspase-3 staining, was unchanged (Supplementary Fig. 6g, h).

Fibroblast volume and clone size increase with stretch

To investigate whether the global rearrangements seen at the population level were reflected in the morphology and behaviour of individual fibroblasts, we used the *PdgfraCreERT2*; *Rosa26*^{Confetti} reporter line at low recombination efficiency to visualise and trace single fibroblasts in the upper dermis (Fig. 5a–d and Supplementary Fig. 7a). Tamoxifen was administered at a low dose (see Methods) on postnatal day (P) 10–12, a time window during which fibroblasts undergo their last rounds of proliferation before entering cell cycle arrest to maintain tissue homoeostasis[21,43]. Mice were subsequently analysed at the adult stage (P60). We leveraged information from CFP+, YFP+ and RFP+ cells not only on clone size, but also on fibroblast volume and shape (clone colour frequency per mouse in Supplementary Fig. 7b). To ensure clonality, we assessed labelling efficiency at 4, 10 and 50 days after low-dose induction (Fig. 5a and Supplementary Fig. 7c). The

https://doi.org/10.1038/s41467-026-73979-0

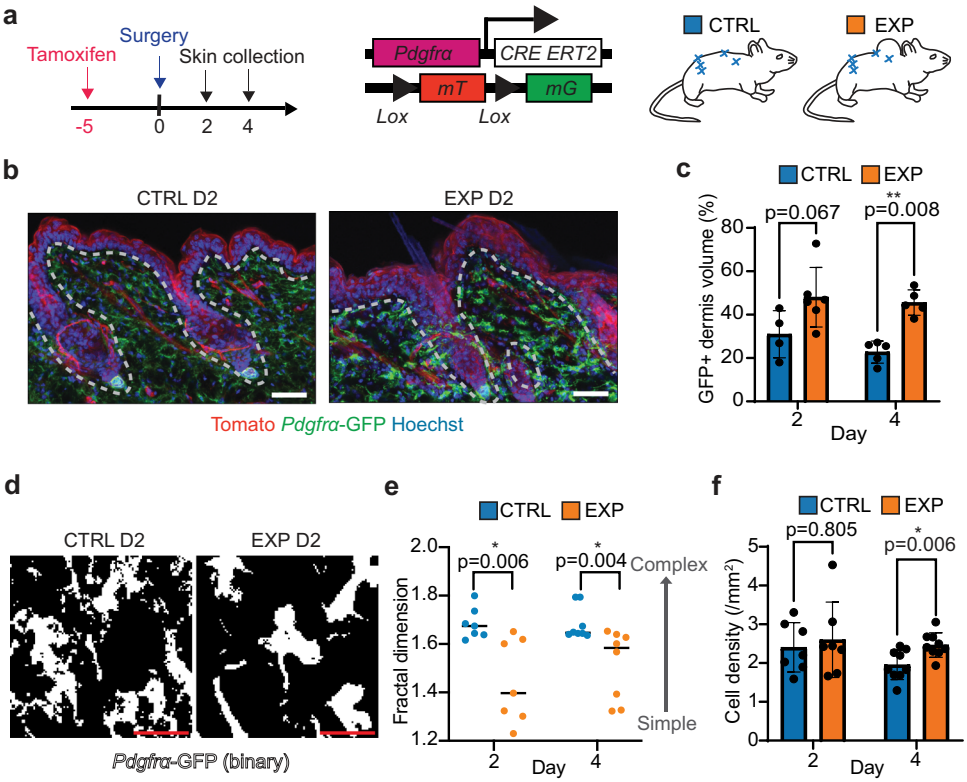

Fig. 4 | Fibroblasts' population-level morphological changes upon expansion. **a** Schematic of the experimental procedure and mouse reporter line used. **b** Fluorescence for Tomato (red), *Pdgfrα*-GFP (green) and Hoechst (blue) in D2 CTRL and EXP skin. Dotted lines are used to delimit the epidermis and hair follicles from the dermis. Only the upper region of the dermis is displayed. Scale bars = 50 µm. **c** Quantification of *Pdgfrα*-GFP volume in the upper dermis based on (**b**). Unpaired two-tailed Mann-Whitney U-tests, $n = 4$ CTRL D2, $n = 5$ CTRL D4, $n = 6$ EXP D2, $n = 5$ EXP D4 mice, dots represent means of 3 measurements per animal. Data are presented as mean +/− standard deviation (SD). **d** Representative binary images of *Pdgfrα*-GFP signal (white) from (**b**) used for fractal dimension quantification. Scale bars = 20 µm. **e** Fractal dimension quantification of fibroblast organisation complexity. Unpaired two-tailed Mann-Whitney U-tests, $n = 7$ mice per condition at D2 and $n = 8$ mice per condition at D4. Data are presented as individual points and the average. **f** Quantification of total cell density in the upper dermis. Unpaired two-tailed Mann-Whitney U-tests, $n = 7$ CTRL D2, $n = 7$ CTRL D4, $n = 9$ EXP D2, $n = 9$ EXP D4 mice, averages of 3 measurements per animal are plotted. Data are presented as mean +/− SD. Source Data are provided as a Source Data file.

majority of observed clones comprised 1 cell, and clone size remained mostly unchanged in non-intervened mice (Supplementary Fig. 7d, e). Throughout the time course, we observed a range of clone sizes (Fig. 5b–e and Supplementary Fig. 7f–h) with a significant increase in clone sizes at D4 post-surgery in the EXP condition (Fig. 5e) and with a clone persistence, calculated as the number of clones per analysed tissue area, that was stable during the time course of the experiment (Supplementary Fig. 7e). The constant persistence with the increase in clone size suggested that more fibroblasts were generated during the tissue expansion procedure.

It has previously been found that upon loss of fibroblasts due to ageing or wounding, remaining fibroblasts are able to compensate for the loss by extending their membranes into depleted areas[44]. We sought to assess whether fibroblasts changed shape upon expansion and found the shape of fibroblasts (assessed by sphericity) was highly heterogeneous in both CTRL and EXP skin (Supplementary Fig. 7i), however the volumes of clones and individual fibroblasts were increased 2 and 4 days after stretching (Fig. 5f, g). Our data indicate that fibroblasts increase their volume on an individual level upon expansion to compensate for the generation of extra dermis, but also highlight an increase in the clone size, suggesting that an increased number of fibroblasts were produced in response to stretching.

ECM downregulation with enhanced fibroblast proliferation

The morphological changes observed in fibroblasts during expansion prompted us to examine the transcriptional alterations associated with their secretory and structural function. In general, in the scRNA-seq data, fibroblasts showed downregulation of genes associated with main components of the ECM, such as *Col1a1*, *Col1a2*, *Col3a1*, *Col4a1*, *Fn1*, *Lum*, *Fbn1*, *Eln*, *Sparc* and *Fbln1* (Fig. 6a, Supplementary Fig. 8a–c and Supplementary Data 5). To further investigate the transcriptional response of fibroblasts to stretching and expansion, and to complement our scRNA-seq analysis with higher sensitivity for low-abundance transcripts, we performed bulk RNA sequencing of FACS-sorted fibroblasts as described previously (Supplementary Fig. 5d). At D1, 440 genes were upregulated and 882 downregulated, at D2, 805 genes were upregulated and 538 downregulated, and at D4, 843 genes were upregulated and 703 downregulated compared to the corresponding controls (Supplementary Fig. 8d, e and Supplementary Data 6). These results are comparable to the differentially expressed genes obtained from our scRNA-seq analysis restricted to the fibroblasts subclusters (Supplementary Fig. 8f, g and Supplementary Data 7). Gene ontology (GO) analysis, based on our bulk RNA-seq data, revealed a downregulation of collagen trimer-related genes (Fig. 6b), and upregulation of genes involved in mitosis (Fig. 6c and Supplementary Data 8). The downregulation of fibrillar collagen I during expansion was confirmed by multiphoton confocal microscopy, via the acquisition of second harmonic generation (SHG) signal at D4 in the upper dermis (Fig. 6d, e). In addition, more than 20 upregulated genes were related to sterol biosynthesis (Supplementary Fig. 8h–k). Given the general membrane remodelling of the entire fibroblast population and the increase in volume of the individual fibroblasts during expansion, the

https://doi.org/10.1038/s41467-026-73979-0

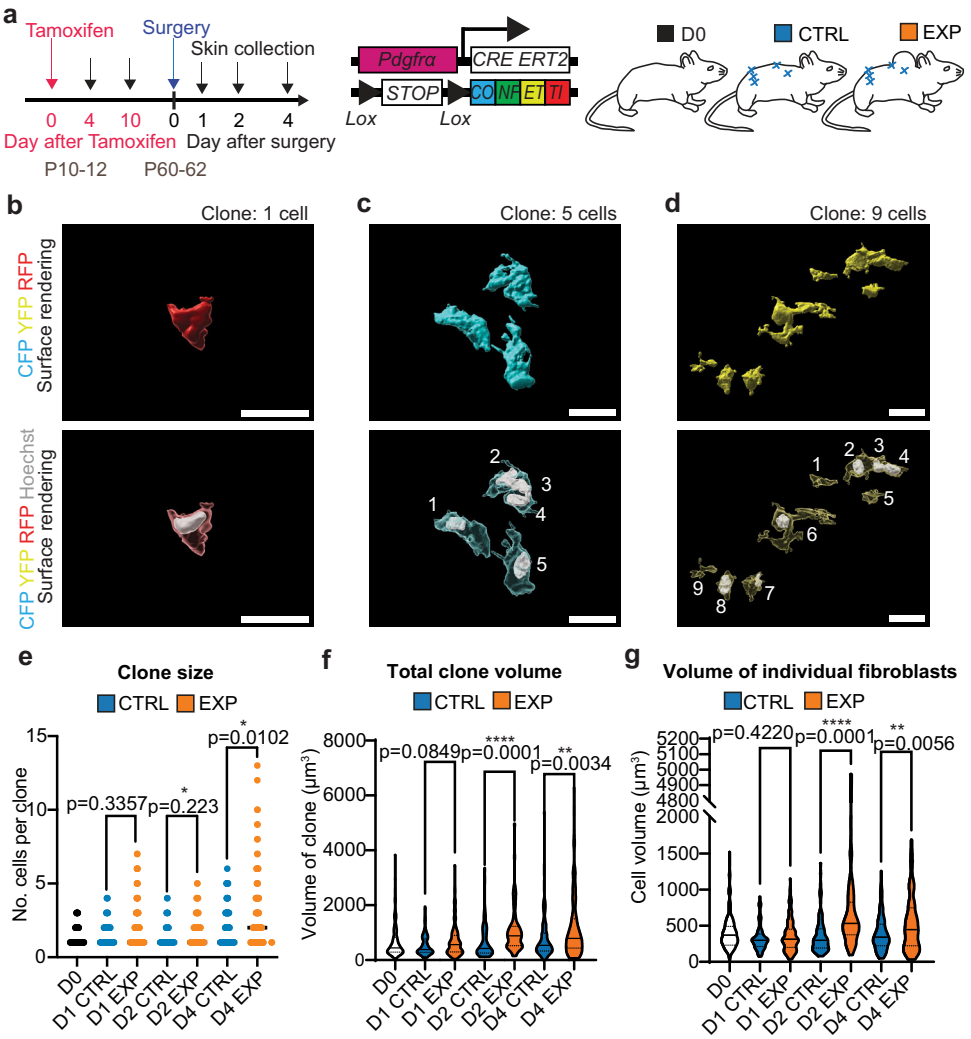

Fig. 5 | Individual fibroblast morphological changes upon expansion. **a** Schematic of the experimental procedure and mouse reporter line used. **b**–**d** Representative images showing surface rendering of Confetti CFP, YFP and RFP (cyan, yellow and red) and Hoechst (white) fluorescence signal from *PdgfraCre-ERT2*; *Rosa26Confetti* wholemounts, generated in Imaris. Scale bars = 20 µm. In the bottom images, the numbers indicate the count of individual cells per clone. These cells were obtained from the upper region of the dermis. **e** Quantification of clone sizes. Unpaired two-tailed Mann-Whitney U-tests, $n = 3$-4 mice per condition (number of measurements for D0 = 99, D1 CTRL = 73, D1 EXP = 124, D2 CTRL = 59, D2 EXP = 77, D4 CTRL = 118, D4 EXP = 125). **f** Quantification of the volume of clones. Unpaired two-tailed Mann-Whitney U-tests, $n = 3$-4 mice per condition (number of measurements for D0 = 99, D1 CTRL = 73, D1 EXP = 124, D2 CTRL = 59, D2 EXP = 77, D4 CTRL = 118, D4 EXP = 125). Data are presented as violin plots showing the median and upper and lower quartiles. **g** Quantification of the volume of individual fibroblasts. Unpaired two-tailed Mann-Whitney U-tests, $n = 3$-4 mice (number of measurements for D0 = 166, D1 CTRL = 90, D1 EXP = 198, D2 CTRL = 95, D2 EXP = 107, D4 CTRL = 175, D4 EXP = 180). Data are presented as violin plots showing the median and upper and lower quartiles. Source Data are provided as a Source Data file.

upregulation of genes related to sterol biosynthesis might be the consequence of cell membrane remodelling. Other upregulated GO terms were related to ribosome biogenesis genes (Supplementary Fig. 8l), changes in Wnt signalling-related genes (Supplementary Fig. 8m and Supplementary Data 9), as well as upregulation of YAP/TAZ targets (Supplementary Fig. 8n). The YAP/TAZ pathway is important in mechanosignalling[45] and is upregulated in keratinocytes upon expansion[15,17]. The nuclear localisation of YAP was confirmed by immunostaining at D4 in the upper dermis, as well as the upregulation of YAP target gene *Ctgf* by qPCR (Supplementary Fig. 8o–q). Given these results, and as lower levels of collagen have previously been associated with fibroblast proliferation during development[46], we investigated the fibroblast proliferation during expansion. In the scRNA-seq data, the increased expression of genes associated with proliferation, such as *Pcna*, *Nasp*, *Slbp* and *Ctcf* (Fig. 6a), led to the prediction that the proportion of fibroblasts in S phase was increased at all three time points in EXP (Supplementary Fig. 8r). We then evaluated proliferation in the upper dermis by assessing 5-Bromo-2′deoxyuridine (BrdU) incorporation (Fig. 6f, g). The percentage of BrdU+ cells increased twofold during expansion at D4 (Fig. 6g), indicating that fibroblasts re-enter the cell cycle. Together, these data suggest that fibroblasts respond to stretching by decreasing ECM production and increasing proliferation. The proliferative behaviour and the reduced collagen expression are characteristic of immature fibroblasts[46,47], prior to their entry into quiescence after post-natal day 10 (P10)[30,43] in the mouse dorsal skin.

In expansion fibroblasts shift towards embryonic-like traits

To support these findings, we compared fibroblast scRNA-seq data from the EXP and CTRL conditions with two distinct transcriptional profiles of mouse embryonic fibroblasts[48,49] (Fig. 6h–k). Using genes enriched in embryonic fibroblasts from mouse skin identified in Jacob

https://doi.org/10.1038/s41467-026-73979-0

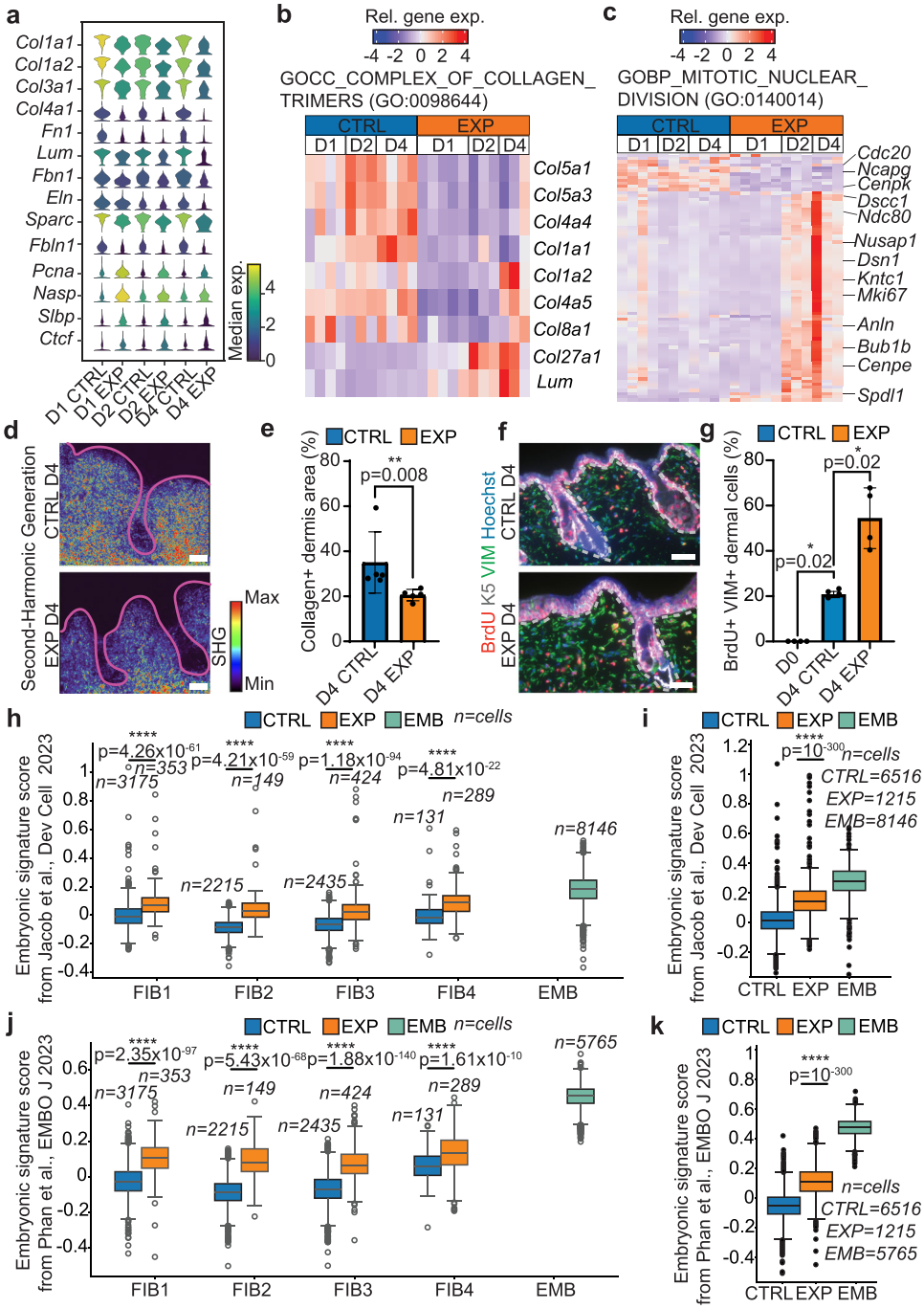

Fig. 6 | Downregulation of ECM genes upon expansion and upregulation of proliferation. a Stacked violin plot of differentially expressed genes (DEG) in scRNA-seq of fibroblasts and fibroblast-like cells. **b**, **c** Heatmaps of DEG from fibroblasts bulk RNA-seq. Relative gene expression (Rel. gene exp.) for the indicated gene ontology (GO) term. Red indicates high expression, blue indicates low expression. **d** Second harmonic generation (SHG) imaging visualising collagen I fibres at D4. Pink lines show the location of the epidermis and hair follicles. The signal intensity is colour coded with red indicating high intensity, blue indicating low intensity, and black indicating no signal. Scale bars = 50 µm. **e** Quantification of SHG area in the upper dermis from (**d**). Unpaired two-tailed Mann-Whitney U-test, $n = 5$ mice per condition, the averages of 3 measurements per animal are plotted. Data are mean +/− SD. **f** Immunofluorescence for BrdU (red), KRT5 (white), VIM (green) and Hoechst (blue) on D4 CTRL and EXP skin. White lines delimit the dermis from the epidermis and hair follicles. Scale bars = 50 µm. **g** Quantification of VIM+ and BrdU+ cells from (**f**) and from mice without surgery (D0). Unpaired one-tailed Mann-Whitney U-test, $n = 4$ mice per condition, averages of 3 measurements per animal shown. Data are mean +/− SD. **h**, **i** Embryonic gene signature scores for FIB1-4 subclusters in CTRL and EXP, compared to the embryonic (EMB) signature from Jacob et al., Dev Cell 2023. Boxplots show median (centre line), interquartile range (box) and 1.5xIQR (whiskers). Two-sided Mann-Whitney U test comparing EXP versus CTRL within each subcluster (per-cell), with Benjamini-Hochberg FDR correction across the four subclusters (**h**). Two-sided Mann-Whitney U test (per-cell, single comparison, **i**). **j**, **k** Embryonic gene signature scores for FIB1-4 subclusters in CTRL and EXP, compared to the EMB signature from Phan et al., EMBO J 2023. Boxplots show median (centre line), interquartile range (box) and 1.5 x IQR (whiskers). Two-sided Mann-Whitney U test comparing EXP versus CTRL within each subcluster (per-cell), with Benjamini-Hochberg FDR correction across the four subclusters (**j**). Two-sided Mann-Whitney U test (per-cell, single comparison, **k**). Source Data are provided as a Source Data file.

https://doi.org/10.1038/s41467-026-73979-0

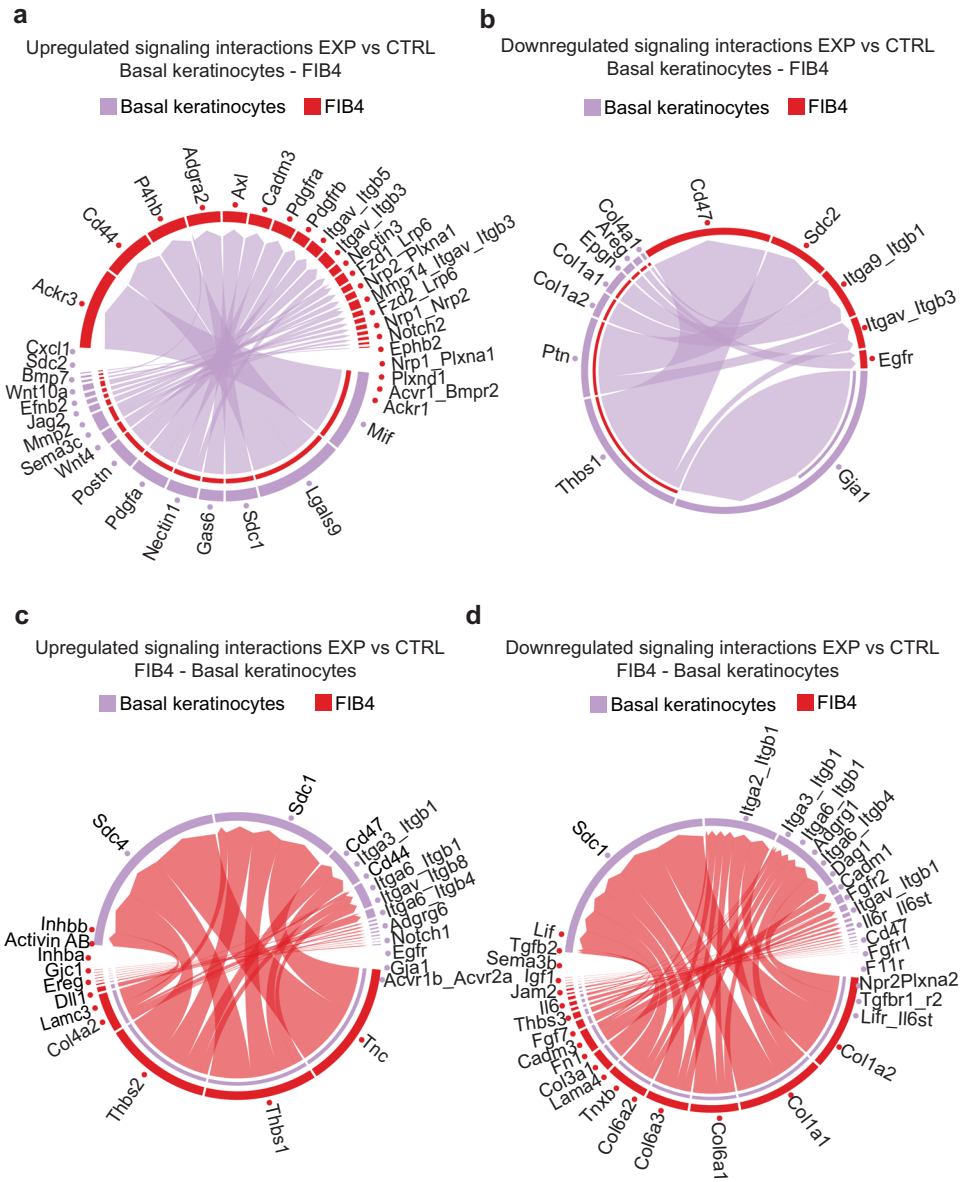

Fig. 7 | Expansion rewires basal keratinocyte to fibroblast communication. **a**, **b** Chord diagrams of predicted ligand-receptor interactions from basal keratinocytes to FIB4 fibroblasts that are upregulated (**a**) or downregulated (**b**) in EXP relative to CTRL. Nodes denote ligand and receptor genes in the sending and receiving populations, chords connect ligand-receptor pairs, and chord thickness reflects relative interaction weight. The size of the diagrams is proportional to the number of interactions. **c**, **d** Chord diagrams of predicted ligand-receptor interactions from FIB4 fibroblasts to basal keratinocytes that are upregulated (**c**) or downregulated (**d**) in EXP relative to CTRL. The size of the diagrams is proportional to the number of interactions.

et al.[48] (Supplementary Data 10), we computed an "embryonic gene signature" score on our dataset. Comparisons were performed considering the FIB1-4 subclusters separately (Fig. 6h) and all fibroblasts together (Fig. 6i). Fibroblasts in the EXP condition display significantly higher embryonic signature score compared to the CTRL, and this is consistent throughout FIB1-4 subclusters (all p-values < 0.001, Fig. 6h). Moreover, we observe the same effect when we analyse all fibroblast clusters together ($p < 0.001$, Fig. 6i). To validate this outcome, we reanalysed our data utilising another independent dataset published in Phan et al.[49], where the authors profile dermal fibroblasts at embryonic day (E14)[49] (Supplementary Data 11). Following the same logic, we re-scored our dataset. Similar to what we observed in the previous analysis, we detected a significantly higher score in fibroblasts under the EXP condition (all p-values < 0.001, Fig. 6j, k). These results demonstrate that EXP fibroblasts acquire a unique ECM composition, gene expression signature and behaviour that resembles developmentally active fibroblasts.

In silico analysis of keratinocyte-fibroblast interactions

To shed light on the cues that may coordinate keratinocyte–fibroblast communication during expansion, we performed a focused ligand–receptor interaction analysis. We specifically examined interactions between basal keratinocytes and the FIB4 population, as this fibroblast cluster is highly enriched in EXP samples (Fig. 1e, f and Supplementary Fig. 2d–h) and is located in close proximity to the epidermis (Fig. 2a–c). In the basal keratinocyte -> FIB4 direction, expansion induced a marked increase in signalling interactions associated with growth factor and mechanosensitive pathways (Fig. 7a). Upregulated ligand-receptor pairs included components of the TGF-β, WNT, and EGF pathways, all of which are known to regulate fibroblast

activation, plasticity, and extracellular matrix remodelling (Supplementary Data 12). These signals suggest that basal keratinocytes actively instruct adjacent fibroblasts during expansion, promoting a transcriptional state consistent with regeneration and tissue remodelling. In contrast, several interactions were downregulated in the expanded condition (Fig. 7b), including signalling mediated by specific ECM components, adhesion molecules, and selected cytokines (Supplementary Data 13). This downregulation indicates that stretch does not simply amplify all epidermal-mesenchymal communication, but rather selectively rewires the signalling landscape, potentially reducing homeostatic or stabilising cues while favouring expansion programmes. Reciprocal analysis of the FIB4 -> basal keratinocyte direction revealed substantial remodelling of fibroblast-derived signals during expansion (Fig. 7c). In the expanded condition, FIB4 cells exhibited increased signalling through pathways associated with ECM dynamics, morphogen signalling, and growth factor availability (Supplementary Data 12). Notably, ligands such as *Tnc*, *Thbs1*, and other matrix-associated factor genes that are transcriptionally upregulated in FIB4 fibroblasts during expansion were predicted to engage receptors expressed by basal keratinocytes. At the same time, signalling via laminins and collagens (*Lama4*, *Col1a1*, *Col1a2*, *Col6a1*, ...) to integrins (*Itga6*, *Itgb1*, *Itgb4*) was reduced (Fig. 7d and Supplementary Data 13), suggesting a shift away from stable adhesion and differentiation cues, in favour of promoting basal keratinocyte self-renewal.

Fibroblasts support keratinocyte self-renewal in expansion

Keratinocytes and fibroblasts engage in reciprocal interactions both in vivo and in vitro[22,47,50,51]. Stretching enhances epidermal stem cells self-renewal[15], prompting us to hypothesise that fibroblasts provide signals that promote this shift in cell fate. To directly test the contribution of fibroblasts to the keratinocyte proliferative potential, we employed a well-established in vitro co-culture system of fibroblasts and human keratinocytes. Since the 1970s, ex vivo expanded human primary keratinocytes have been extensively used in clinical settings for treating burn patients, corneal reconstruction, and gene therapy for genetic skin disorders like epidermolysis bullosa[52–55]. Successful long-term epidermal regeneration is guaranteed by the presence of a sufficient pool of self-renewing epidermal stem cells in the graft[54]. The self-renewal capacity of these cells is strongly influenced by the culture conditions, which traditionally rely on a clinical-grade clone of lethally irradiated 3T3-J2 embryonic fibroblasts serving as a mitotically inactive feeder layer (FL)[22]. Keratinocyte stem cells undergo long-term expansion only when seeded on the FL and maintained in a specialised medium[56]. To determine whether the FL support is mediated primarily by soluble factors or instead requires physical interactions, we first tested whether the FL secretome alone could sustain keratinocytes proliferation (Supplementary Fig. 9a). Human primary keratinocytes were expanded using the standard FL method (SQ-FL) or cultured without FL either in fresh medium (FM) or in FL-conditioned medium (CM-SQ) (Supplementary Fig. 9a–d). Keratinocytes cultured on SQ-FL retained robust proliferative potential over many passages (Supplementary Fig. 9b–d-orange line). In contrast, keratinocytes grown without a FL, either in FM (grey lines) or CM-SQ (brown lines), rapidly lost proliferative capacity within a few passages (Supplementary Fig. 9b–d) and showed reduced expression of stemness-associated markers, including TP63 and FOXM1[56] and an increase in differentiation markers such as Involucrin (IVL) (Supplementary Fig. 9e). Collectively, these results indicate that feeder-derived soluble factors alone are insufficient to sustain robust keratinocyte expansion.

We next compared two fibroblast preparations that differ in the time they remain in culture after irradiation before being used as FL for the keratinocytes. In the standard protocol, the FL is used within 24 h (standard-quality FL, SQ-FL). We contrasted this with a FL that is left in culture for 4 days before use (low-quality FL, LQ-FL) (Fig. 8a). During serial cultivation, keratinocytes grown on LQ-FL display reduced clonogenicity, an increased percentage of aborted colonies, and fewer cells at sub-confluence compared to cells cultured on SQ-FL (Fig. 8b–e). Consistently, analysis of stem cell markers at both RNA and protein levels revealed a decrease in their expression, accompanied by a modest increase in differentiation markers (Fig. 8f, g). Notably, correcting the number of fibroblasts plated under LQ conditions (LQ-ADJ) did not rescue keratinocyte proliferation (Supplementary Fig. 9f, g). To identify features underlying the FL phenotype and assess intrinsic differences between SQ-FL and LQ-FL, we profiled both the secretome (Supplementary Fig. 9h) and the total proteome using mass-spectrometry–based proteomics. Relative to fresh medium, SQ-FL secreted 548 proteins (Supplementary Fig. 10a and Supplementary Data 14) enriched for elastic-fibre organisation and integrin-mediated interactions (Supplementary Fig. 10a–c). Comparison of SQ-FL and LQ-FL secretome showed only small differences (42 and 44 differentially expressed proteins at 6 h and 16 h, respectively), mainly associated with collagen/elastic-fibres organisation and chemokine signalling (Supplementary Fig. 10d–j and Supplementary Data 15). Comparing intracellular proteins by mass spectrometry, the SQ-FL had lower abundance of ECM-associated proteins, including collagens, and higher levels of proteins linked to cell proliferation compared to LQ-FL (Fig. 9a–d and Supplementary Fig. 11a–d). We confirmed these differences in COL4A1 and FN1 by western blot analysis (Fig. 9e) and by immunostaining (Fig. 9f, g and Supplementary Fig. 11e). While FL thickness did not differ appreciably between conditions (Supplementary Fig. 11f, g), the SQ-FL was significantly softer than LQ-FL as measured by Atomic Force Microscopy (AFM) (Fig. 9h–j). The gene set enrichment analysis (GSEA) revealed downregulation of pathways associated with ECM organisation in SQ-FL relative to LQ-FL (Fig. 9k and Supplementary Fig. 11h). In the SQ-FL cell cycle features were upregulated (Fig. 9l and Supplementary Fig. 11h). Importantly, we did not detect enrichment of stress- or apoptosis-related pathways, consistent with X-ray–irradiated fibroblasts adopting a stable, non-lethal mitotic arrest (Supplementary Data 16) Moreover, the gene expression analysis reveals that the SQ-FL cells exhibit transcriptional profile more similar to the in vivo EXP condition (Supplementary Fig. 11i). Together these data indicate that downregulation of ECM and upregulation of markers associated with a proliferative signature in fibroblasts play a role in promoting the self-renewal of epidermal stem cells.

ECM control of holoclone-forming keratinocyte stem cells

During in vitro culture, human primary keratinocytes generate holoclones, meroclones and paraclones[1]. Holoclone-forming cells are long-lived stem cells that give rise to the other clonal colony types and ultimately to terminally differentiated cells. Because this hierarchy places holoclones at the root of keratinocyte renewal, we asked whether FL ECM features influence this stem cell behaviour. We performed scRNA-seq on primary keratinocytes after four passages on SQ-FL or LQ-FL. Unsupervised clustering identified five keratinocyte states as previously reported[56] (Fig. 10a). Cultures maintained on SQ-FL contained a higher fraction of cells within the holoclone-associated cluster (17.6%) compared with cultures grown on LQ-FL (12.2%), whereas the proportions of meroclone/paraclone-associated clusters remained largely stable and differentiated populations increased under LQ conditions (Fig. 10a–e). This data confirmed that the proliferation and self-renewal capacity of human keratinocytes is dependent on the characteristics of the fibroblasts they are cultured on.

Discussion

We have generated a transcriptomic atlas of stretch-mediated expansion in mouse back skin. We have demonstrated that fibroblasts sense mechanical stretching in vivo and ultimately respond by decreasing their production of ECM and re-entering the cell cycle, reverting to a "young" fibroblast cell state[43,46,57]. Finally, we have shown that this

https://doi.org/10.1038/s41467-026-73979-0

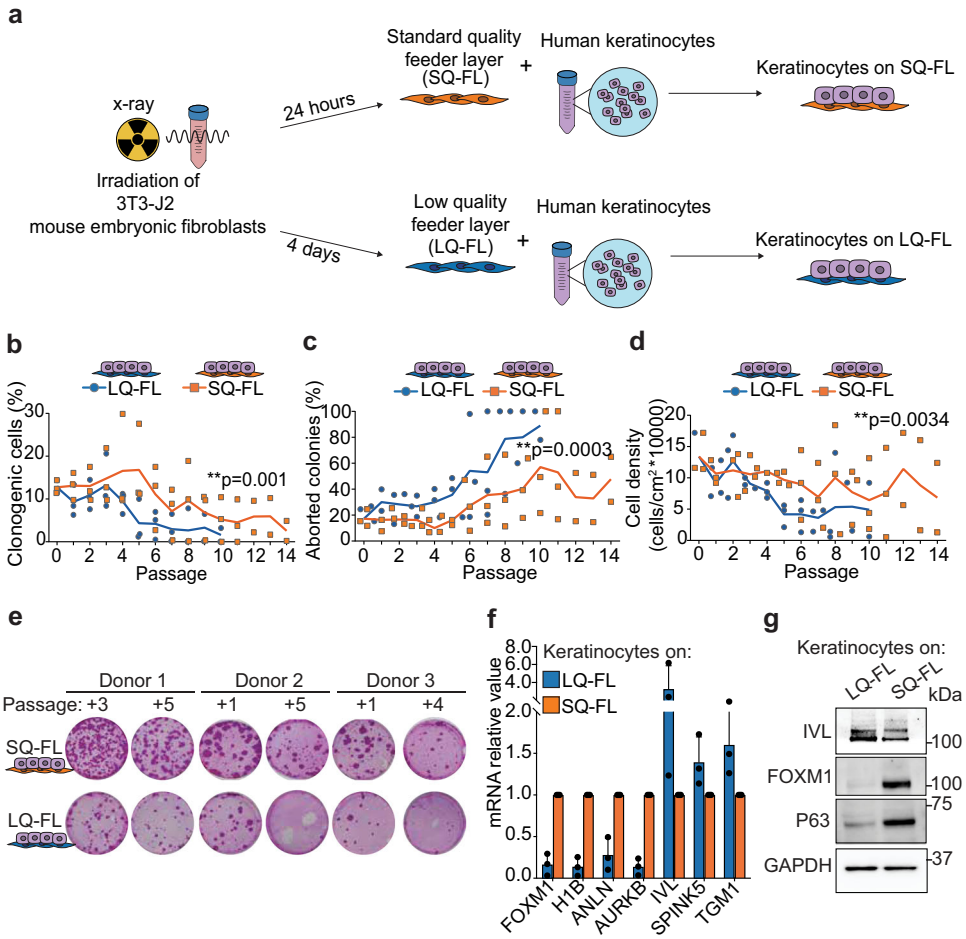

Fig. 8 | Fibroblast-keratinocyte interactions are important for keratinocyte proliferation. a Schematic diagram of the co-culture system of human primary keratinocytes on a feeder layer made by a clone of x-ray irradiated 3T3-J2 fibroblast. **b**, **c** Serial cultivation of normal human keratinocytes on LQ-FL (blue line) and SQ-FL (orange line). The percentage of clonogenic cells was calculated as the ratio between grown colonies and plated cells (**b**). The percentage of aborted colonies was calculated as the ratio between the colonies scored as aborted and the number of clonogenic cells (**c**). Two-tailed paired Student *t* test, $n = 3$ independent biological replicates. Data are presented as mean +/− SEM. **d** Total amount of cells obtained at sub-confluence during serial cultivation of normal human keratinocytes on LQ-FL (blue line) and SQ-FL (orange line). Two-tailed paired Student *t* test, $n = 3$ independent biological replicates. Data are presented as mean +/− SEM. **e** Representative images related to (**b**–**d**) showing the indicator dishes derived from keratinocytes cultured on SQ-FL or LQ-FL at the indicated passage. **f** qRT-PCR quantification of the mRNA levels of clonogenic markers (*FOXM1, H1B, ANLN, AURKB*) and differentiation markers (*IVL, SPINK5, TGM1*) on three human primary keratinocytes cultures grown on SQ-FL (orange bars) and LQ-FL (blue bars). Non-parametric Mann-Whitney test, *FOXM1* $^*p = 0.040$, *H1B* $^*p = 0.033$, *ANLN* $p = 0.094$, *AURKB* $^*p = 0.031$, *IVL* $p = 0.327$, *SPINK5* $p = 0.327$, *TGM1* $p = 0.327$. $n = 3$ independent biological replicates. Data are presented as mean +/− SD. **g** Western analysis of total cell extracts from cultures generated by human primary keratinocytes grown on SQ-FL and LQ-FL. One out of three representative experiments is shown. Source Data are provided as a Source Data file.

behaviour is important in vivo but also during in vitro epidermal expansion, promoting the proliferation of epidermal stem cells, potentially coupling the response of dermal and epidermal compartments during expansion.

Fibroblast heterogeneity has been described in many contexts[26,58]. Two main fibroblast lineages, papillary and reticular, have been identified in mouse[43,49] and in human[59,60]. Fibroblast transcriptional heterogeneity has also been described previously, in early development[48], during homoeostasis in mouse[24], as well as in human skin[61,62], and in other contexts, such as wound repair[28,42,63–65], cancer[66], ageing[29] and UV damage[67]. Here we show transcriptional changes during expansion, as well as changes in protein expression. In recent years, spatial transcriptomics datasets of skin have been published[68,69]. Here, we have coupled scRNA-seq and spatial transcriptomics to map the locations of fibroblast subtypes and show that fibroblast cellular heterogeneity is associated with specific spatial niches.

While mechanical stretch has been implicated in wound healing[70], where it operates alongside injury-induced inflammatory and repair programmes, our expansion model isolates stretch in the absence of wounding, revealing that fibroblast ECM downregulation and cell-cycle re-entry, together with pro-proliferative cues to keratinocytes, are direct consequences of mechanical load rather than secondary to tissue injury.

ECM plays an important role in cellular behaviour in various contexts, such as development and tumour initiation. Fibroblasts are proliferative in prenatal skin and enter a quiescent state in postnatal skin, which coincides with an increase in collagen deposition[46]. ECM can also influence epithelial progenitor cell behaviour, as observed during postnatal development of sebaceous glands[71]. Collagen levels can affect tumour initiation as well[72]. We observed lower expression of extracellular matrix genes, including collagens, and decreased mature collagen fibres at the protein level in the in vivo EXP condition. From the scRNA-seq data, we observed increased cellular proliferation in the expanded condition. These findings coincide with an increase in clone sizes at D4 post-surgery in the EXP condition via lineage tracing. The subsequent BrdU

https://doi.org/10.1038/s41467-026-73979-0

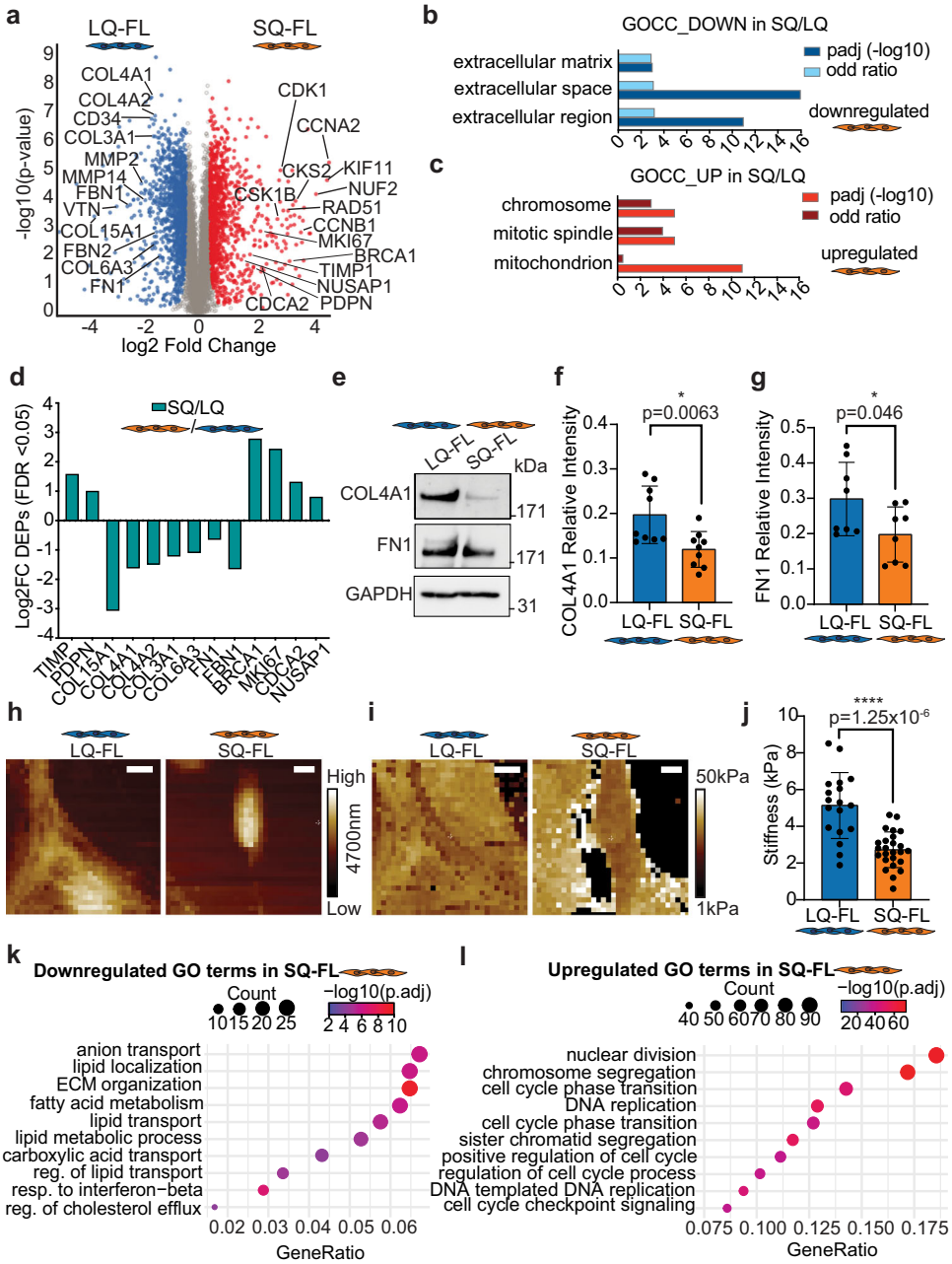

Fig. 9 | Low-ECM expressing fibroblasts support keratinocytes growth. **a** Volcano plot of the proteins identified by mass spectrometry analysis of standard quality feeder layers (SQ-FL) compared to low quality feeder layers (LQ-FL). Downregulated proteins are in blue, upregulated proteins are in red. X-axis shows fold-change (log2(ratio)), y-axis shows statistical significance as −log10 of the Benjamini–Hochberg–adjusted *p*-value (*q*-value, FDR = 0.05). **b** Downregulated cellular component terms in SQ-FL compared to LQ-FL. Data are −log10 of the corrected *p* value (dark blue) and corresponding fold changes (light blue). **c** Upregulated cellular component terms in SQ-FL compared to LQ-FL. Data are −log10 of the corrected *p* value (red) and corresponding fold changes (dark red). **d** Log2 fold change of the indicated proteins of interest. **e** Western blot of total cell extracts from SQ-FL and LQ-FL. **f**, **g** Quantification of staining intensity related to Supplementary Fig. 11e for COL4A1 (**f**) and FN1 (**g**). Data are mean +/− SD. 9 (**f**) or 8 (**g**) measures from $n = 1$ representative experiment. **h** Example of a topographic image from the Force Volume data at constant force. The vertical position of the sample is tracked when the force set point is reached. **i** Map of the Young Modulus (Log scale) of the Force Volume image obtained from a fit of all curves using the Sneddon model. The black region around cells (top-right) corresponds to the rigid substrate. **j** Distribution of Young´s modulus. For each cell, multiple force curves were extracted from the Force-Volume images. The extraction regions were chosen based on the corresponding topographic images and correspond to the central region of each cell. Data are mean +/− SD. Unpaired t-test. 18 (LQ-FL) and 25 (SQ-FL) measures from $n = 1$ representative experiment. **k**, **l** GO Biological Process enrichment of differentially expressed genes in SQ-FL versus LQ-FL bulk RNA-seq ($n = 4$ biological replicates per condition), shown separately for downregulated (**k**) and upregulated (**l**) genes. Dot size indicates gene count, colour indicates -log10(padj), and the x-axis shows GeneRatio. One-sided hypergeometric test with Benjamini-Hochberg correction. Source Data are provided as a Source Data file.

incorporation analysis further confirmed this, indicating that the increase in cell density in the dermis is due to the proliferation of fibroblasts. However, we cannot rule out that there is also migration of cells from the fascia[40,41] as we did not trace these populations.

The coordination of different cell types is essential for maintaining the skin's architecture, integrity, and its barrier function. Many interactions have been described between cell populations in the skin during homoeostasis[68,73–76] and in wound healing[77]. Aberrant interactions can lead to diseases such as psoriasis[78,79]. Crosstalk can also be

https://doi.org/10.1038/s41467-026-73979-0

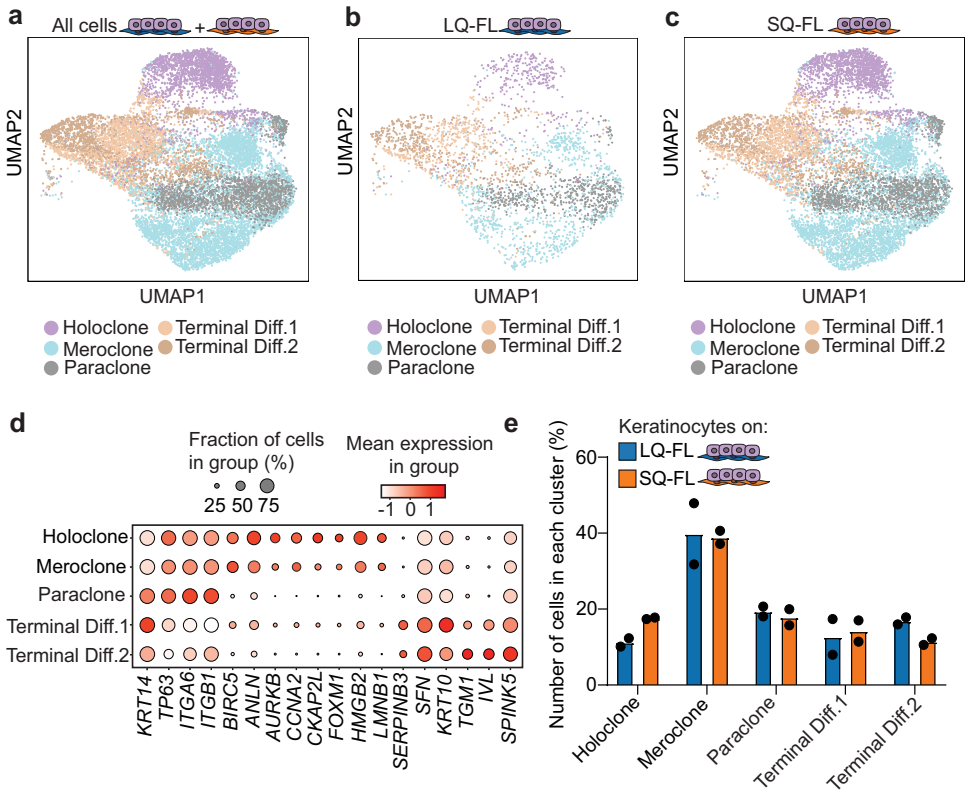

Fig. 10 | Single-cell analysis of human primary keratinocytes growth on SQ and LQ feeder layer. a UMAP projections of all human keratinocytes from LQ-FL (2777 cells, $n = 2$) and SQ-FL (10,336 cells, $n = 2$) feeder conditions, coloured by cell type. **b** UMAP of human keratinocyte cells cultured on LQ-FL, coloured by predicted cell type. **c** UMAP of human keratinocyte cells cultured on SQ-FL, coloured by predicted cell type. **d** Marker gene expression for each of the indicated clusters. **e** Proportion of each keratinocyte cell type cultured on LQ-FL versus SQ-FL ($n = 2$). Bars show mean proportions across biological replicates, dots represent individual replicates. Source Data are provided as a Source Data file.

indirect, via ECM remodelling[80]. For example, basement membrane remodelling is essential during mouse embryogenesis and interaction between the ECM and cells is required for cell polarisation and morphogenesis[80]. It has also been reported that lower substrate stiffness results in increased proliferation of keratinocytes in culture[81–83]. Here, we identify the fibroblasts transcriptional changes associated with keratinocyte proliferation in both in vivo and in vitro expansion.

Understanding the interactions required for stretch-mediated expansion could allow for an increased rate of growth by targeting pathways involved, thus reducing the months of discomfort patients experience with expanders in place. This study paves the way for future research into the roles of different cell types in coordinating the maintenance of tissue architecture upon expansion. In addition, current in vitro production of grafts for clinical application is limited to the growth of epidermal sheets[54,55]. A deeper understanding of how cell types interact to maintain tissue architecture will improve the production of organised full skin for regenerative therapies.

Methods

Animals

The experiments were approved by the Animal Experiments Inspectorate in Denmark, under license number 2021-15-0201-00792. All experiments were performed with male mice of age postnatal day (P) 60-P90, unless otherwise indicated. All animals were housed in specific pathogen-free animal facilities, in either open or individually ventilated cages that were placed under a 12 h light–dark cycle at ambient temperature and humidity. Mice had access to food and water ad libitum. *PdgfraCre-ERT2* mice[84] were obtained from Kim B. Jensen (University of Copenhagen) with permission from Brigid Hogan (Duke University Medical Centre). *Rosa26*^{Confetti} reporter mice[85] were obtained from Kim B. Jensen (University of Copenhagen), and *Rosa26*^{mTmG} reporter mice[86] were obtained from Henrik Semb (University of Copenhagen). Mice are on a mixed genetic background. Where not otherwise specified, SWISS mice (Janvier Labs) were used. Animal euthanasia was performed with cervical dislocation accordingly to ethical approval.

Expander experiments

Surgery was performed as described previously[15]. Briefly, mice were anaesthetised with 5% xylazine and 10% ketamine in phosphate-buffered saline (PBS) through intraperitoneal injection (200 µL/30 g mouse). The back skin was shaved, and mice were injected subcutaneously with a local painkiller, carprofen (5 mg/kg), near the incision site. Skin was disinfected with iso-betadine (Meda Pharma) prior to making an incision on the back skin close to the tail. A subcutaneous path from the incision site to the neck region was created using forceps, and a self-inflating 4 mL sphere tissue expander (Osmed) was then placed subcutaneously near the neck region. The expanders were kept in place by 3 stitches, and the incision site was stitched closed. For CTRL mice, the same procedure was followed, minus the expander insertion.

Lineage tracing experiments

To induce recombination in fluorescent reporter lines, mice were injected intraperitoneally with Tamoxifen (T5648, Sigma-Aldrich) dissolved in corn oil (10616051, Thermo Scientific Chemicals). *Pdgfra-CreERT2;Rosa26*^{mTmG} were injected once 5 days prior to surgery, approximately at P60, with 5 mg of tamoxifen per 30 g mouse. *PdgfraCre-ERT2; Rosa26*^{Confetti} mice were injected once between P10-P12

with 0.05 mg of tamoxifen per 4 g mouse. We term D0 mice as those that did not receive surgery.

Clonal analysis

Cells were assigned to the same clone only if they were less than 50 μm apart, and only clones that were clearly separated from neighbouring clones were included in the analysis. To ensure clonality, we analysed only animals in which the labelling efficiency, calculated by quantifying the number of labelled cells within a defined area, was maintained below 2% on average. Clone persistence was normalised by dividing the number of clones per image by the area of skin imaged. The area of skin was determined by producing maximum intensity projections of z-stack images and measuring the area manually in ImageJ.

Proliferation experiments

Mice were injected twice a day following expander surgery with 5-Bromo-2′-deoxyuridine (BrdU) (B5002, Sigma-Aldrich) dissolved in PBS. A dose of 2 mg per 30 g mouse was given each time. BrdU was also given in drinking water at a concentration of 1 mg/mL.

Isolation of live skin cells and fibroblasts

Digestion of skin tissue was performed as previously described[30]. Briefly, the skin was shaved, dissected, and minced into small pieces using scissors. The minced tissue was placed in a solution of 2.5 mg/mL Collagenase I (C0130, Sigma-Aldrich) and 0.01 M $CaCl_2$ (423525000, Thermo Scientific Chemicals) in HBSS (14025100, ThermoFisher Scientific) and incubated at 37 °C for 2 h on a shaker. The digestion was stopped by the addition of 5 mM EDTA (15575020, ThermoFisher Scientific), the suspensions were filtered through 40 μm strainers and then centrifuged to obtain cell pellets.

For the isolation of live single cells for scRNA-seq, cells were stained with 4′,6-diamidino-2phenylindole, dihydrochloride (DAPI) (D1306, ThermoFisher Scientific, 0.3 mM). Each sample was also stained with hashing antibodies (TotalSeq™-A03XX anti-mouse Hashtag, BioLegend, 1:100, Supplementary Table 3) for 20 min in order to be able to distinguish them once pooled for sequencing. Live cells were sorted into eppendorfs using a BD FACSAria II or BD FACSymphony S6 cell sorter (BD Biosciences), with a 70 μm nozzle.

To sort for fibroblasts for qPCR and bulk RNA sequencing, staining was performed for 30 minutes with primary antibodies, followed by washing with PBS, staining for 30 min with secondary antibodies (where required) and washing again. The antibodies used were CD45-PE (12-0451-82, Invitrogen, 1:1200), CD31-PE (553373, BD Biosciences, 1:2000), CD117-PE (553355, BD Biosciences, 1:4000), EPCAM-PE (118205, BioLegend, 1:800), PDGFRA-APC (17-1401-81, Invitrogen, 1:100), CD34-Biotin (14-0341-82, Invitrogen, 1:50) and StrepAlexaFluor750 (S21384, Invitrogen, 1:400). Cells were also stained with 0.3 mM DAPI. Sorting was performed using a BD FACSAria II sorter (BD Biosciences) with a 100 μm nozzle. Cells were sorted into Eppendorf tubes and flash frozen in liquid nitrogen.

Single-cell RNA sequencing

Per sequencing round, we had 2 samples for library preparation – one sample containing pooled control cells and the other containing pooled expanded cells. Single-cell libraries were generated using the Chromium Next GEM Single Cell 3′ Reagent Kits v3.1 (Dual Index) (10X Genomics) following the manufacturer's protocol, with additional steps due to hashing (Supplementary Table 3) as described previously[87,88]. Briefly, a primer (HTO primer, 0.2 mM) was added during the amplification of cDNA to increase the amplification of hashtag barcodes. Following amplification, the hashtag cDNA was separated from the sample cDNA using SPRIselect beads (Beckman Coulter). 30 ng of hashtag cDNA was then amplified using the Kapa HiFi HotStart Ready Mix (KK2601, Roche) plus SI-PCR primer (10x Genomics, 0.17 μM) and unique Illumina TruSeq index primers (Illumina, 0.17 μM). Hashtag-related primer sequences can be found in the Supplementary Table 3. All libraries were diluted to 4 nm. The control and expanded cDNA libraries were pooled with their respective hashtag libraries at a ratio of 95:5. Subsequently, these two were pooled at a 50:50 ratio per sequencing round.

Sequencing was carried out with a P2 100 kit on a NextSeq2000 sequencer (Illumina).

Single-cell RNA sequencing analysis

Sequencing reads were aligned to the mm10-2020-A reference genome using CellRanger (v.6.1.2) with default parameters. Filtered count matrices for each sample were subsequently loaded using Scanpy[89] (v.1.9.3). Cell hashing (Supplementary Table 3) antibody demultiplexing was performed using Seurat[90] (v.4.3.0), with hashtag-derived oligonucleotides (HTOs) normalised using centred log ratio (CLR) normalisation. Demultiplexing was conducted with the HTODemux function, setting the positive quantile to 0.99. Quality control and preprocessing were performed on each individual sample with Scanpy. For each sample, cells passed the following criteria: had more than 500 detected genes, showed expression of fewer than 15% mitochondrial genes, and were not identified as outliers in other metrics using a median absolute deviation (MAD) threshold of 5. Doublets were identified using scDblFinder[91] (v.1.8.0) in R (v.4.1.3) with default parameters. Cells classified as doublets were removed from further analysis. Normalisation was performed by scaling the total counts to the same level for each cell, followed by log1p-transformation. Highly variable genes were selected across batches using Scanpy, taking into account the batch information with the cell-ranger method, retaining the top 5000 variable features. Principal component analysis was performed on normalised data to reduce dimensionality prior to batch correction. Data from different time points and conditions were integrated using HarmonyPy[92] (v.0.0.9) to correct for batch effects. After this integration, the neighbourhood graph was computed based on the Harmony-corrected principal components for downstream analysis. Leiden clustering was performed at multiple resolutions, with 0.2 chosen for further analysis. Marker genes for each cluster were identified using a Wilcoxon rank-sum test as implemented in Scanpy's rank_genes_groups function, requiring at least 25% of cells in the cluster to express the marker. Clusters were annotated using known marker genes and manual curation based on prior biological knowledge of mouse skin cell types. Fibroblasts identified in the initial clustering were subset and re-clustered at multiple resolutions. Subclusters were annotated as distinct fibroblast subtypes, and marker genes were recalculated to refine subpopulation identification. Differential gene expression analysis was performed using the MAST method[93] in Seurat to investigate differences between both conditions (CTRL vs. EXP), across time points, and for each time point separately. Cell cycle scoring was conducted using Seurat to assign cells into different cell cycle phases. Human cell cycle genes were converted to mouse orthologs using gprofiler2, and cell cycle phases were assigned using CellCycleScoring based on S and G2M phase markers. Cell-cell communication was inferred using CellChat (v2.1.2)[94]. CellChat objects were created for control and expanded conditions separately, with cell type identities transferred from the Seurat metadata, and subsetted to the two cell populations of interest: Fibroblast 4, and keratinocytes_basal. Communication probabilities were computed using the triMean method, and ligand-receptor pairs supported by fewer than 10 cells per group were excluded. The two condition-specific objects were merged for comparative analysis. Differentially expressed ligand-receptor pairs between conditions were identified using a Wilcoxon rank-sum test (thresh.pc = 0.1, thresh.fc = 0.05, $p < 0.05$), and mapped onto inferred communications using netMappingDEG. Up-regulated pairs in the expanded condition were defined by a ligand logFC > 0.05, and down-regulated pairs by a ligand logFC < − 0.05. Chord diagrams visualising directional signalling changes between Fibroblast 4 and

keratinocytes_basal were generated using netVisual_chord_gene and exported as SVG files.

Spatial transcriptomics

Spatial transcriptomics was performed on sections of D2 control skin using the Xenium platform (10X Genomics) following the manufacturer's protocol at KU Leuven Institute for Single Cell Omics (Leuven, Belgium). A custom panel of 95 genes plus the Xenium Mouse Tissue Atlassing panel (Supplementary Data 17) was run to detect mRNA transcripts. Skin from four mice was used, with 3 technical replicates.

Spatial transcriptomics analysis

A custom probe set, combined with the Xenium Mouse Tissue Atlassing panel (Supplementary Data 17), was designed based on our previously obtained scRNA-seq data. A deep learning approach was used to prioritise cell type identification and capture within-cell-type expression variability, to optimise gene selection for spatial profiling (https://github.com/sifrimlab/Concrete-Geneselection). Slides were analysed using the Xenium analyser (10X Genomics) with instrument software version 2.0.1.0 and analysis version xenium-2.0.0.10, using default settings for cell segmentation, transcript decoding, and assignment. Filtered output files from the instrument's pipeline were used for downstream analysis. Spatial transcriptomics data from 10X Xenium was processed using Scanpy (v.1.9.3). Filtered data was loaded using read_10x_h5(), and metadata was integrated. Quality control metrics were computed, and cells with fewer than 10 transcripts were filtered out. Data normalisation was performed by scaling the counts with the normalize_total() function, followed by log(1 + x) transformation. scRNA-seq cell type annotation mapping of the spatial data was performed using an adaptation of the PopV package[95] (v.0.4.2), which incorporates multiple annotation methods such as scVI, scANVI,Scanorama, Harmony, and others[92,96,97]. In addition, two widely used annotation transfer tools, Tangram[98] and DotR[99], were applied as well, both with default parameters for high-resolution data. For integration, 10,000 cells per reference cell type were sampled when possible. The final merged spatial dataset contained 85,344 cells and 474 genes. Consensus cell typing, which relies on combining the results of multiple annotation methods to increase accuracy and confidence, was then calculated, and cells for which two or more methods agreed on an annotation were annotated. To calculate fibroblast distances from the epidermis, the interfollicular epidermis was manually annotated. The minimum distance of each cell to the closest epidermis cell was then calculated using the cdist function from scipy.spatial.distance (SciPy v.1.14.1)[100], applying the Euclidean distance metric. Distances were computed separately for each sample. Density plots were generated by dividing the spatial tissue area into bins, averaging the raw expression values for all spots within each bin, and normalising these averaged values to a scale of 0 to 1 to allow comparability across samples for the same gene.

Bulk RNA-seq

RNA was extracted from sorted cells using the RNeasy® Micro Kit (74004, QIAGEN), following the manufacturer's protocol. Ultra-Low Input RNA-seq was performed using the Illumina platform (2x150bp) at GENEWIZ (Azenta Life Sciences, New Jersey, USA).

Analysis was performed using R. FASTQ files were aligned to the mouse genome mm39, and counts calculated using RSubread[101]. The counts table was filtered to include only genes where count numbers were 14 or more in at least 3 samples using edgeR[102]. Differential expression analysis was performed using the DESeq2 package[103], keeping only differentially expressed genes with a p-value of < 0.05 and a fold change greater than 1.5 or less than −1.5. Gene set enrichment analysis was done using fgsea. Gene lists from gene ontology and Reactome terms were obtained from the MSigDB[104,105] database using the msigdbr package. To generate heatmaps, gene lists from selected GO and Reactome terms were filtered to include only genes we found to be differentially expressed in our dataset. Heatmaps showing scaled normalised counts of these genes were generated using ComplexHeatmap[106].

qPCR on mouse tissue

Following RNA extraction using the RNeasy® Micro Kit, cDNA synthesis was performed using the High-Capacity cDNA Reverse Transcription Kit (4368814, ThermoFisher Scientific) following the manufacturer's protocol. The qPCR reaction was performed using the SolisFAST® SolisGreen® qPCR Kit (Solis BioDyne) according to the manufacturer's instructions and run on a QuantStudio™ 7 Pro Real-Time PCR System (Applied Biosystems). Primer sequences are below and additional information are in Supplementary Data 18: *B2m* CTCGGTGACCCTGGTCTTTC (5′–3′), GGATTTCAATGTGAGGCGGG (5′–3′);

Cd34 AGGCTGATGCTGGTGCTAG (5′–3′), AGTCTTTCGGGAATAGCTCTG (5′–3′);

Ctgf(*Ccn2*) GAAGCTGACCTGGAGGAAAA (5′–3′), ACTGGCAGAGTGGTGGTTCT (5′–3′);

Fdft1 TCCCTGACGTCCTCACCTAC (5′–3′), CCCCTTCCGAATCTTCACTA (5′–3′);

Gapdh TGCCAGCCTCGTCCCGTAG (5′–3′), CGGCCTTGACTGTGCCGTTG (5′–3′);

Mmp13 CAGTCTCCGAGGAGAAACTATGAT (5′–3′), GGACTTTGTCAAAAAGAGCTCAG (5′–3′);

Pdpn AGATAAGAAAGATGGCTTGC (5′–3′), AACAACAATGAAGATCCCTC (5′–3′);

Sqle AGTTCGCTGCCTTCTCGGATA (5′–3′), GCTCCTGTTAATGTCGTTTCTGA (5′–3′);

Timp1 CGAGACCACCTTATACCAGCG (5′–3′), GGCGTACCGGATATCTGCG (5′–3′);

Tnc TCCCCAAGAGAATTTACAGCTACAG (5′–3′), AGATTCATAGACCAGGAGGTATCCA (5′–3′).

Relative fold changes in gene expression of samples (run in triplicate) were calculated using the delta-delta Ct method[107] (ΔΔCt) and normalised to the housekeeping gene *B2m*.

Mouse tissue preparation, cryosectioning and immunostaining

After dissection, skin samples containing endogenous fluorescence were fixed for 3 hours at room temperature (RT) with 4% PFA (P6148, Sigma-Aldrich) prior to washing and embedding in OCT. Samples without endogenous fluorescence were directly embedded in OCT. Blocks were flash frozen by submersion in Iso-Pentane (10121820, Fisher Chemical), which was cooled to − 150 °C using liquid nitrogen. Cryosectioning was performed with a HM 560 CryoStar (Thermo Scientific) or CM1950 (Leica Biosystems) at − 25 °C. Standard sections were cut at a thickness of 8 µm. For analyses of *Pdgfrα-CreERT2;Rosa*^{mTmG} and SHG/collagen, wholemount sections of 50 µm were cut, and for *PdgfraCre-ERT2; Rosa26*^{Confetti} sections of 200 µm.

Standard tissue sections were fixed (if the tissue was not already fixed prior to embedding) for 10 min at RT with 4% PFA, followed by washing 3 times in PBS for 5 min. Tissues were blocked for 1 h at RT with slide blocking buffer (1% BSA (BP9702-100), 5% horse serum (26-050-088, Gibco), 0.2% Triton X-100 (X100, Sigma-Aldrich) in PBS). Slides were incubated with primary antibodies overnight at 4 °C. Slides were washed 3 times in PBS for 5 min, followed by incubation with secondary antibodies for 1 h at RT. Slides were washed again in PBS. For BrdU staining, slides were incubated post-fixation in 1 N HCl for 30 minutes at 37 °C, followed by washing for 3 times in PBS for 10 minutes before continuing with the staining protocol as described. The following primary antibodies were used: anti-CD104 (Integrin β4) (553745, BD Biosciences, 1:200), anti-KRT5 (905901, Biolegend, 1:1000), anti-Vimentin (ab92547, Abcam, 1:2000), anti-Vimentin (ab24525, Abcam, 1:500), anti-TNC (AB19011, Sigma-Aldrich, 1:100),

anti-PDPN (ab11936, Abcam, 1:80), anti-YAP (14074, Cell Signalling Technology, 1:50), anti-CD34 (ab81289, Abcam, 1:200), anti-BrdU (ab6326, Abcam, 1:200) and anti-cleaved Caspase-3 (9661, Cell Signalling Technology, 1:100). The following secondary antibodies (Jackson Immunoresearch) were used at a 1:400 dilution: anti-rabbit, anti-chicken, anti-rat conjugated to Rhodamine Red-X, Alexa Fluor 488, Alexa Fluor A647, or Cy5. Nuclei were stained with Hoechst (H3570, ThermoFisher Scientific, 1:1000).

Wholemount tissue sections were blocked for 1 h at RT with wholemount blocking buffer (1% BSA, 5% horse serum, 0.8% Triton X-100 in PBS), followed by incubation with Hoechst (1:1000) for 3 h at RT and washing with PBS 3 times for 5 min.

For both standard sections and wholemounts, cover slides were mounted with 2.5% 1,4Diazabicyclo[2.2.2]octane (D27802, Sigma-Aldrich) in Glycerol Mounting Medium (C0563, Dako).

Mouse skin imaging

Z-stack images of wholemounts were acquired using laser-scanning confocal microscopes (LSM 780 (ZEISS), LSM 880 Airyscan (ZEISS) or Stellaris (Leica Biosystems)). To acquire images of collagens using second harmonic generation, a multiphoton microscope was used (SP8 Multiphoton (Leica Biosystems)). Images of standard 8 µm sections were acquired with a widefield microscope (DM5500 (Leica Biosystems)).

Image analysis

PdgfrαCre-ERT2;Rosa26^{mTmG} analysis. Volume quantifications were performed with the image analysis software Imaris (Oxford Instruments) by masking the *Pdgfrα*-GFP signal to produce 3D surfaces. To account for the larger volume of skin in the expanded condition, GFP volumes from the EXP condition were normalised by multiplying by a factor of 2 at D2 and 2.15 at D4. These values correspond to the measured increase in expander radius from D0 to D2 and D0 to D4[15].

PdgfrαCre-ERT2; Rosa26^{Confetti} analysis. Quantifications of cell volume and sphericity were performed in Imaris by masking the fluorescence signal to produce surfaces. For clonal analysis, clones were defined as surfaces within a 50 µm distance from each other. Surfaces with multiple nuclei were counted as multiple cells within the same clone. Incomplete cells were also counted if their volume exceeded 100 µm^3. Plots of individual fibroblast volume and sphericity show data only from individual cells (surfaces with 1 nucleus).

Other analyses. Quantifications of cell numbers were performed manually in ImageJ. Quantifications of signal area and fractal dimension using FracLac[42] were also performed in ImageJ on binary images.

Dermal thickness was measured using QuPath[108].

Quantification of fluorescence signals from immunostainings (PDPN, TNC, PDGFRA, CD34, cCasp3, YAP, and BrdU) and fluorescent proteins (GFP, Tomato) was performed in ImageJ. The positive signal was measured as the area covered by the staining and normalised to the total analysed area. For TNC quantification, vessel-like structures were excluded by subtracting the area occupied by these structures from the analysis.

Human tissues

All human tissue samples were obtained with informed consent for research use, adhering to Italian regulatory standards (Ethics Committee of the Area Vasta Emilia Nord, approval number 178/09 for healthy donor skin samples). The donors did not receive any compensation for providing tissue samples.

3T3-J2 cell line used as feeder layer

Mouse 3T3-J2 cells, originally provided by Professor Howard Green from Harvard Medical School (Boston, MA, USA), were cultured in DMEM with 10% gamma-irradiated adult bovine serum, penicillin–streptomycin (50 IU/ml), and 4 mM glutamine.

Primary human cell cultures from healthy donors

Primary human keratinocytes were seeded at 0.6×10^4 cells/cm^2 onto X-ray–irradiated, mitotically inactivated 3T3-J2 feeder cells and cultured at 37 °C in a humidified atmosphere with 5% CO_2. The keratinocyte growth medium (KGM) consisted of a 2:1 mixture of Dulbecco's Modified Eagle's Medium (DMEM) and Ham's F12, supplemented with 10% fetal bovine serum (FBS), 50 IU/ml penicillin–streptomycin, 4 mM glutamine, 0.18 mM adenine, 5 µg/ml insulin, 0.1 nM cholera toxin, 0.4 µg/ml hydrocortisone, 2 nM triiodothyronine (liothyronine sodium), and 10 ng/ml epidermal growth factor (EGF). Cells were serially passaged at sub-confluence until senescence. Under the fresh medium (FM) condition, keratinocytes were cultured on plastic surfaces without 3T3-J2 feeder cells using freshly prepared KGM. In the conditioned medium (CM) condition, keratinocytes were cultured on plastic without feeder cells in KGM preconditioned for 24 h by lethally irradiated 3T3-J2 cells seeded at 2.8×10^4 cells/cm^2. In the standard-quality feeder layer (SQ-FL) condition, 3.0×10^4 X-ray–irradiated fibroblasts/cm^2 were seeded to obtain a density of 2.8×10^4 cells/cm^2 24 hours after seeding, corresponding to the time of keratinocyte expansion. In the low-quality feeder layer (LQ-FL) condition, 3.0×10^4 X-ray–irradiated fibroblasts/cm^2 were seeded to obtain a density of 2.4×10^4 cells/cm^2 4 days after seeding, corresponding to the time of keratinocyte expansion. In the adjusted low-quality feeder layer (LQ-ADJ-FL) condition, 3.6×10^4 X-ray–irradiated fibroblasts/cm^2 were seeded to obtain a density of 2.8×10^4 cells/cm^2 4 days after seeding, corresponding to the time of keratinocyte expansion.

Colony-forming efficiency

The colony-forming efficiency of keratinocytes during each culture expansion was assessed by plating between 1000 and 5000 cells in parallel on indicator dishes and staining with rhodamine B after 12 days. The total number of colonies was expressed as a percentage of the cells initially seeded. Aborted colonies, consisting of large, flattened, terminally differentiated cells, were quantified as a percentage of the total colonies.

Western blot analysis

Keratinocytes and fibroblasts were harvested by scraping in 1 x RIPA buffer (Sigma Aldrich) with phosphatase and protease inhibitor cocktails (Thermo Fisher). Total protein concentrations were determined using Pierce BCA Protein Assay Kits (Thermo Fisher Scientific). Equal amounts of protein were separated on 4–12% NuPAGE Bis-Tris Gels or 3–8% NuPAGE Tris Acetate Gels and transferred onto nitrocellulose membranes (Millipore) at 100 V for 2 hours at 4 °C. Membranes were blocked with Everyblot Blocking Solution (Bio-Rad). Primary antibodies were incubated overnight at 4 °C or 2 h at RT. The following primary antibodies were used: anti-IVL 1:5000 from Invitrogen (Ma1-25752, mouse), anti-FOXM1 1:1000 from Cell Signalling Technologies (D3f2b, rabbit), anti-P63α 1:1000 from Cell Signalling Technologies (4892 s, rabbit), anti-GAPDH 1:500 from Sigma-Aldrich (Zrb374, rabbit), anti-COL4A1 1:1000 from Rockland (600-101-MN4, Goat), anti-FN1 from Proteintech 1:10000 (66042-1-Ig, Mouse), anti-GAPDH 1:500 from Abcam (ab8245, mouse). Secondary antibodies were applied for 1 hour at RT. The following antibodies were used: goat pAb to rabbit IgG (HRP) 1:1000-5000 from Abcam (Ab205718), rabbit pAb to Goat IgG (HRP) 1:2500 from Abcam (Ab6741), and goat pAb to mouse IgG (HRP) 1:20000 from Abcam (Ab6789). Signals were detected using Clarity Western ECL Substrate (Bio-Rad) and visualised with a ChemiDoc system (Bio-Rad) using ImageLab software.

Immunostaining and image analysis of feeder layer

Irradiated 3T3-J2 cells were plated onto glass coverslips and fixed with PFA 3% for 10 min at room temperature after 24 h (SQ-FL) and 4 days

(LQ-FL). Cells were then carefully washed with PBS. Permeabilization was performed in PBS/Triton-X 0.5% for 20 min at RT. Blocking solution (FBS 5% + BSA 2% in PBS/Triton-X 0.1%) was added for 30 min at 37 °C. Primary antibodies were diluted in blocking solution and added to the samples overnight at 4 °C. The following primary antibodies were used: anti-COL4A1 (600-101-MN4, Rockland, 1:400), anti-FN1 (66042-1-Ig, Proteintech, 1:1000). Secondary antibodies were diluted in Blocking solution and added to the samples for 1 h at RT in the dark. The following secondary antibodies were used: donkey anti-goat IgG (H + L) Alexa Fluor 488™ (A11055, Invitrogen, 1:200) and donkey anti-mouse IgG (H + L) Alexa Fluor 568™ (A10037, Invitrogen, 1:2000). Cell nuclei were stained with DAPI (10236276001, Roche). Dako Fluorescence Mounting medium (S3023, Dako) was used to mount coverslips. Zeiss Axio Imager 2 with 20x objective was used to visualise fluorescent signals and acquire images. Quantification of the intensity of fluorescence was performed on random fields with the image analysis software ImageJ, normalising the mean grey value on the number of nuclei. Phalloidin-Atto 488 (1:100 – 49409 Sigma-Aldrich) was used to stain actin and measure cell thickness with a Z-stack acquisition with Zeiss Axio Observer with 40x objective.

RNA extraction and real-time qPCR on human samples

Total RNA was extracted from cells using the PureLink RNA Mini Kit (Thermo Fisher Scientific) to perform quantitative real-time PCR. cDNA was synthesised with the SuperScript VILO cDNA Synthesis Kit (Thermo Fisher Scientific). Real-time qPCR experiments were conducted in triplicate using retrotranscribed cDNAs with TaqMan Universal PCR Master Mix on the QuantStudio 12k Flex Real-Time PCR System (Thermo Fisher Scientific). Gene expression levels were normalised to GAPDH as the reference gene. The following TaqMan primers (Thermo Fisher Scientific) were used: ANLN Hs01122612_m1, AURKB Hs00945855_g1, FOXM1 Hs01073586_m1, GAPDH 4352665, H1B Hs00271207_s1, IVL Hs00846307_s1, SPINK5 Hs00928570_m1, TGM1 Hs00165929_m1. Data analysis was carried out using RQ Manager Software 1.2.2.

Bulk RNA-seq on SQ and LQ-FL

Total RNA was extracted from cells using the PureLink RNA Mini Kit (Thermo Fisher Scientific). Ultra-Low Input RNA-seq was performed using the Illumina platform. Bulk RNA sequencing data were aligned to the mouse genome (mm39) using STAR[109], and gene-level counts were generated using featureCounts. Downstream analyses were performed in R. Lowly expressed genes were filtered using edgeR[102]. Differential expression analysis was conducted using DESeq2[103]. Differentially expressed genes (DEGs) were defined as those with an adjusted p-value < 0.05 and an absolute $\log_2$ fold change > 1.5. Gene Ontology (GO) Biological Process enrichment analysis was performed using clusterProfiler[110]. Enriched terms with adjusted p-values < 0.05 were visualised using dot plots, where dot size represents gene count and colour represents − log10(FDR).

Single-cell RNA sequencing and analysis on keratinocytes grown on SQ-FL and LQ-FL

For details on single-cell RNA sequencing experiments, refer to ref. 56. Briefly, four keratinocyte cultures, two grown on SQ-FL and two on LQ-FL, were detached with trypsin for 15–20 min and filtered in order to obtain a single cell suspension, pelleted and resuspended in culture medium and in 1 × phosphate-buffered saline (PBS) with 0.04% BSA. 10,000 cells of each sample were loaded into one channel of the Chromium Chip B using the Chromium Next GEM Single Cell 3′ Reagent Kits v3.1 (Dual Index) (10X Genomics). cDNA was synthesised and amplified following the manufacturer's protocol. Sequencing was performed on the Illumina sequencing platform. Filtered gene expression matrices were loaded using the Read10X_h5 function from Seurat[90] (v.4.3.0). Four single-cell datasets were included: two SQ samples and two LQ samples. Each dataset contained both human and mouse genes; only human transcripts were retained by filtering for features with the prefix "GRCh38_". Gene identifiers were cleaned by removing the prefix and Ensembl version numbers. Individual Seurat objects were created for each dataset, and quality control metrics were computed, including the percentage of mitochondrial gene expression. Low-quality or multiplet cells were excluded using interquartile range (IQR) filtering on total gene counts (nFeature_RNA), UMI counts (nCount_RNA), and mitochondrial content (percent.mt < 15%). Each dataset was normalised using log normalisation, and the top 2000 highly variable genes were selected using the "vst" method. Samples were then integrated using Seurat´s anchor-based integration pipeline (v3.1.5 strategy). Integration features were selected across all samples, anchors were identified using canonical correlation analysis (CCA), and a joint object was created using IntegrateData with 30 dimensions. Cell cycle scoring was conducted using Seurat to assign cells into different cell cycle phases. Human cell cycle genes were converted to mouse orthologs using gprofiler2, and cell cycle phases were assigned using CellCycelScoring based on S and G2M phase markers. Dimensionality reduction was conducted using PCA and UMAP (both on 30 dimensions). To annotate cell types, we leveraged a previously integrated reference dataset containing curated cell type labels. Transfer anchors were computed between the reference and query objects using the first 30 PCs. Cell type labels were transferred using the TransferData function, and predicted cell type labels were added to the query object.

Mass spectrometry (MS) sample preparation

SQ and LQ feeder layers were collected by scraping at 24 h (SQ-FL) and 4 days (LQ-FL) after plating and pelleted. In two different experiments, we analysed 2 and 3 samples for each condition. Proteomic sample preparation was performed with the EasyPep MS Sample Prep Kit (Thermo Fisher Scientific) following the manufacturer's instructions. For the first LC-MS experiment, Peptides were separated on a 50 cm µPAC NEO HPLC column (Thermo Scientific), using a Vanquish Neo (Thermo Fisher Scientific) UHPLC. Peptide separation was performed using a 53 min stepped gradient of 4-22.5% solvent B (0.1% formic acid in 80% acetonitrile) for 40 min, 22.5-45% solvent B for 13 min, using a constant flow rate of 350 nL/min. Column temperature was controlled at 50 °C. Upon elution, peptides were injected via a Nanospray Flex ion source and 10-uM emitter (Evosep) into a Tribrid Ascend mass spectrometer (Thermo Scientific). Spray Voltage was set to 2200(V). Data was acquired in data independent mode with the Orbitrap MS resolution 60.000 for full scan range 400–900 m/z, AGC target was 250% and maximum injection time set to auto. 42 DIA scans with 12 Th width and 1 Th overlap spanning a mass range of 400–900 m/z were were acquired at 15,000 MS resolution, AGC target 1000% and maximum injection time of 27 ms. HCD fragmentation normalised collision energy (NCE) was set to 30%. For the second LC-MS experiment, peptides were separated on an Aurora (Gen3) 25 cm, 75 µM ID column packed with C18 beads (1.6 µm) (IonOpticks) using a Vanquish Neo (Thermo Fisher Scientific) UHPLC. Peptide separation was performed using a 50 min stepped gradient of 2–17% solvent B (0.1% formic acid in acetonitrile) for 33 min, 1725% solvent B for 11 min, 25–35% solvent B for 6 min, using a constant flow rate of 400 nL/min. Column temperature was controlled at 50 °C. Upon elution, peptides were injected via an EASY-Spray source into a Tribrid Ascend mass spectrometer (Thermo Scientific). Spray Voltage was set to 1700(V). Data was acquired in data independent mode with the Orbitrap MS resolution 60.000 for full scan range 400–900 m/z, AGC target was 250% and maximum injection time set to auto. 42 DIA scans with 12 Th width and 1 Th overlap spanning a mass range of 400–900 m/z were acquired at 15,000 MS resolution, AGC target 1000% and maximum injection time of 27 ms. HCD fragmentation normalised collision energy (NCE) was set to 30%.

For secretome analysis SQ and LQ-FL murine fibroblast 16 h secretome (FBS-free medium) were pre-treated according to ref. 111, with slight modification. Briefly, 8 mL of cold acetone were added to 2 mL of secretome, incubated for 30 min at room temperature, then centrifuged at 2800 × *g* for 20 min. Protein pellets were washed twice with 95% ethanol, and, after complete ethanol evaporation, the obtained pellets were resuspended in 100 µL of 8 M urea and 20 mM HEPES pH 8. The protein content of each sample was quantified with the BCA assay (Merck & Co, Rahway, New Jersey, U.S.). Each condition was obtained in biological triplicate, and crude medium was used as a negative control for a total of $n = 9$ biological samples, treated in technical replicates. A filter aided sample preparation (FASP) protocol was employed for tryptic digestion before LC-MS analysis. Briefly, the equivalent of 100 µg of protein lysate per sample were loaded on 30kDa Microcon centrifugal filters (Merck & Co, Rahway, New Jersey, U.S.), and reduced with 50 mM DTT (Sigma Adrich, Burlington, Massachusetts, United States). Cysteines were alkylated with 100 µL of a 55 mM aq. iodoacetamide solution (Sigma Aldrich) and digested with 1:80 MS-grade recombinant porcine trypsin (Roche, Basel, Switzerland) overnight in 50 mM ammonium bicarbonate solution. The recovered peptides were desalted with a standard C18 SPE extraction using Pierce Peptide Desalting Spin Columns (Thermo Fisher, Waltham, Massachusetts, U.S.) previously conditioned in 0.1% aqueous trifluoracetic acid (TFA). Peptides were eluted with 0.1% TFA in 50% acetonitrile and dried in a SpeedVac (Eppendorf's, Hamburg, Germany)[112]. Each sample was reconstituted with 80 µL of mobile phase (2% ACN in 0.1% formic acid), and 1 µL was injected on an UltiMate 3000 nano UHPLC coupled to an Orbitrap Exploris 480 Mass Spectrometer, equipped with a nano-ESI source (Thermo Fisher) at Centro Interdipartimentale Grandi Strumenti (UniMoRe). An EASY-Spray 500 mm×75 µm, ID 2 µm, column was employed for sample separation at 200 nL/min in 160 min gradient (2 to 30% ACN in 0.1 % formic acid), with a FullMS-ddMS2 method, DDA top20. Analysis parameters were set as follows: MS1 resolution 120,000, Scan range 370-3000, RF lens 50%, normalised ACG target 300%, MaxIT 120 ms. MS/MS parameters were set as follows: nce 30%, isolation window 1.5 m/z, isolation offset 0.4 m/z, normalised ACG target 200% (120 ms MaxIT). A dynamic exclusion window of 55 s was used throughout all the experiment[113]. In total, three biological replicates were analysed per condition, each digested and injected in duplicate. HeLa whole cell lysate (Abcam, Cambridge Biomedical Campus, Cambridge, UK) was used to assess MS status before sample analysis.

MS data analysis

MS files were processed using DIA-NN v.1.8 in directDIA mode with a library predicted from the mouse Uniprot fasta file (UP000000589) covering 55,079 protein isoforms. Highly heuristic protein grouping and Match between runs (MBR) were turned on. Carbamidomethylation of cysteine was specified as fixed modification, Oxidation of methionine, acetylation at the protein N-terminus, and N-terminal methionine excision were set as variable modifications. Maximum missed cleavage was set to 1, and a maximum of 2 variable modifications were allowed. The minimum peptide amino acid length was 7. The protein groups and precursors were filtered at 1% FDR. All other settings were set as default.

All statistical analysis were performed using Proteomelit 1.0.0, an in-house Python tool, based on the automated analysis pipeline of the Clinical Knowledge Graph[114]. Intensity values were log2-transformed and features with less than 70% of valid values in at least one group were removed. Remaining missing values were imputed using the MinProb approach using a width of 0.3 and downshift of 1.8[115]. Protein significance was assessed through two-tailed unpaired *t* tests with permutation-based False Discovery Rate (FDR) correction for multiple hypothesis testing, where parameters were set to FDR 0.05, Fold-change (FC) 1, s0 1, and 250 permutations. Functional enrichment analysis was performed using Fisher´s exact test and Benjamini-Hochberg correction (FDR 0.05).

For secretome analysis, MS raw data were loaded onto Proteome Discoverer v3.2 platform (Thermo Fisher) and analysed using a standard LFQ analysis. A t-test with Benjamini correction was applied between control replicates and each treatment. Identification was run against a validated M. musculus UniProtKD database (updated on July 2025, 116,662 entries) and cRAP, with an FDR 1 % tolerance on peptide identification (10ppm on MS1, 0.02 Da on MS/MS exact spectra), and Chimerys extension for multiple spectra deconvolution[116,117]. Trypsin was specified as cleaving enzyme (R/K | X cleavage sites (X ≠ P), one missing cleavage admitted). M(oxidation) and N-term acetylation were considered as variable modifications, and C(-carbamidomethylation) as a fixed modification. 10ppm of mass tolerance was applied for precursor ions and 0.02 Da on ms/ms fragments. FDR were controlled using a target-decoy strategy, with thresholds set to 1% at the peptide-spectrum match (PSM), peptide, and protein levels. Quantitation was based on chromatographic peak heights. Protein abundances were normalised across all the samples with total peptide normalisation method, considering only murine-derived proteins. A two-tailed t-test was applied between the SQ/LQ-FL samples and the control groups. Differentially expressed proteins (DEPs) were identified as those proteins with $a - 1.5 \le FC \le 1.5$ (where FC stands for Fold Change and represents log2 of the abundance ratio with respect to control) with a *p*-value < 0.05 between triplicates, corrected with FDR 5 % (BH correction) and expressed as -log(10)adj *p*-value. 1971 proteins derived from 14,907 peptides were initially identified, with 1.01 % of missing cleavages on total cleavage sites (0.99% of which represented by peptides with one missing cleavage site). Further post-analysis filters were introduced to refine software identification, *i.e.* exclusion of proteins with <4% sequence coverage, proteins identified with no unique peptide, and/or with < 2 general peptides. These filters led to the identification of 1528 validated proteins. STRING analysis was used to characterise the secretome interactomes[118]. DEPs for each differential analysis were loaded on STRING (v 12.0) with their FC values, with a confidence score of 0.700 on primary, global networks. Clusters were then generated according to Markov Cluster algorithm (MCL) with inflation parameter set to 3 to discriminate the most represented GO:MF and GO:BP subclasses[119]. To compare the degree of similarity between SQ-FL vs control sample (KGMNC, non-conditioned KGM media) and SQ vs LQ-FL secretome DEPs at 16 h, PANTHER Functional Classification System (v 19.0, https://www.pantherdb.org/) was used based on primary level GO: BP analysis.

Stiffness measurement with atomic force microscopy (AFM) on SQ and LQ-FL

Force curves on SQ and LQ-FL, plated in p35 petri dishes, were acquired with a Bioscope AFM microscope equipped with a Nanoscope IIIA controller (Veeco Metrology, Plainview, NY, USA). A custom temperature-controlled stage was used to keep the cells at 37 °C during the measurements. To provide for the lack of a CO_2 environment, HEPES was added to the cell culture medium to reach a total of 25 mM and the analysis time kept below 2 h for each petri dish. Force curves were acquired with DNP silicon nitride cantilever/ pyramidal tips (Bruker, USA) with a nominal spring constant of 0.12 N/m. The cantilever spring constant was calibrated according to the thermal noise method[120]. To account for the strong spatial heterogeneity of cell mechanical properties, for each analysed cell a Force Volume image was acquired and then only force curves from a rectangular area cantered on the nucleus of the cells were analysed and the results were averaged to provide a single value for each cell. The vertical cantilever speed was kept lower than 2 µm/s to reduce as much as possible viscous contributions in the obtained value of the Young modulus. Cell indentation was limited to 300–400 nm to avoid the contribution from the underlying rigid substrate. Force curves were fitted using the

Sneddon modified Hertz model[121] exploiting the NanoScope Analysis 1.5 Software (Bruker, USA).

Statistics and reproducibility

When not otherwise specified, all statistical tests were calculated using GraphPad Prism 10. Statistical significance was defined as $p < 0.05$. The statistical tests used are indicated in the figure legends. For all experiments, normality was tested using D'Agostino & Pearson tests. When normality tests were not passed, nonparametric statistical tests were performed, namely Mann-Whitney U-tests. For human culture and western blot experiments, two-tailed Student *t* tests were used when normality was assessed positively. For mass spectrometry experiments, significance was calculated using Fisher´s exact tests and correction for multiple tests was performed using the Benjamini-Hochberg method. No statistical method was used to predetermine sample size. No data were excluded from the analyses. The experiments were not randomised. The investigators were not blinded to allocation during experiments and outcome assessment.

Reporting summary

Further information on research design is available in the Nature Portfolio Reporting Summary linked to this article.

Data availability

Data supporting the findings of this study are available within the article (and its Supplementary Information and Tables) and from the corresponding authors. The accession number for the mouse scRNA-seq data in GEO is GSE285079. The accession number for the mouse bulk RNA-seq data in GEO is GSE284808. The accession number for the human keratinocytes scRNA-seq and feeder layer bulk RNA-seq data in GEO is GSE324558. The mass spectrometry proteomics data have been deposited to the ProteomeXchange Consortium via the PRIDE partner repository with the dataset identifier PXD078047 and PXD078052, and JPOST with the dataset identifier PXD077441. Source data are provided in this paper.

Code availability

Codes are available at https://github.com/sifrimlab/Aguilera-et-al/.

References

1. Nguyen, T. M. & Aragona, M. Regulation of tissue architecture and stem cell dynamics to sustain homeostasis and repair in the skin epidermis. *Semin. Cell Dev. Biol.* **130**, 79–89 (2022).
2. Iskratsch, T., Wolfenson, H. & Sheetz, M. P. Appreciating force and shape-the rise of mechanotransduction in cell biology. *Nat. Rev. Mol. Cell Biol.* **15**, 825–833 (2014).
3. Mammoto, T., Mammoto, A. & Ingber, D. E. Mechanobiology and developmental control. *Annu. Rev. Cell Dev. Biol.* **29**, 27–61 (2013).
4. LeGoff, L. & Lecuit, T. Mechanical Forces and Growth in Animal Tissues. *Cold Spring Harb. Perspect. Biol.* **8**, a019232 (2015).
5. Dupont, S. & Wickstrom, S. A. Mechanical regulation of chromatin and transcription. *Nat. Rev. Genet.* **23**, 624–643 (2022).
6. Guillot, C. & Lecuit, T. Mechanics of epithelial tissue homeostasis and morphogenesis. *Science* **340**, 1185–1189 (2013).
7. Vining, K. H. & Mooney, D. J. Mechanical forces direct stem cell behaviour in development and regeneration. *Nat. Rev. Mol. Cell Biol.* **18**, 728–742 (2017).
8. Kirby, T. J. & Lammerding, J. Emerging views of the nucleus as a cellular mechanosensor. *Nat. Cell Biol.* **20**, 373–381 (2018).
9. DuFort, C. C., Paszek, M. J. & Weaver, V. M. Balancing forces: architectural control of mechanotransduction. *Nat. Rev. Mol. Cell Biol.* **12**, 308–319 (2011).
10. Zollner, A. M., Holland, M. A., Honda, K. S., Gosain, A. K. & Kuhl, E. Growth on demand: reviewing the mechanobiology of stretched skin. *J. Mech. Behav. Biomed. Mater.* **28**, 495–509 (2013).
11. Tzolova, N. & Hadjiiski, O. Tissue expansion used as a method of reconstructive surgery in childhood. *Ann. Burns Fire Disasters* **21**, 23–30 (2008).
12. Cho, M. J. et al. The current use of tissue expanders in breast reconstruction: device design, features, and technical considerations. *Expert Rev. Med. Devices* **21**, 27–35 (2024).
13. Biggs, L. C., Kim, C. S., Miroshnikova, Y. A. & Wickstrom, S. A. Mechanical Forces in the Skin: Roles in Tissue Architecture, Stability, and Function. *J. Invest. Dermatol.* **140**, 284–290 (2020).
14. Villeneuve, C. et al. Mechanical forces across compartments coordinate cell shape and fate transitions to generate tissue architecture. *Nat. Cell Biol.* **26**, 207–218 (2024).
15. Aragona, M. et al. Mechanisms of stretch-mediated skin expansion at single-cell resolution. *Nature* **584**, 268–273 (2020).
16. Chu, S. Y. et al. Mechanical stretch induces hair regeneration through the alternative activation of macrophages. *Nat. Commun.* **10**, 1524 (2019).
17. Xue, Y. et al. Mechanical tension mobilizes Lgr6(+) epidermal stem cells to drive skin growth. *Sci. Adv.* **8**, eabl8698 (2022).
18. Ding, J. et al. Macrophages are necessary for skin regeneration during tissue expansion. *J. Transl. Med.* **17**, 36 (2019).
19. Liu, Y. et al. IL-11 Drives dermal fibroblast activation in mechanical stretch-mediated skin expansion. *J. Invest. Dermatol.*https://doi.org/10.1016/j.jid.2025.07.023 (2025).
20. Xue, Y. et al. The mechanotransducer Piezo1 coordinates metabolism and inflammation to promote skin growth. *Nat. Commun.* **16**, 6876 (2025).
21. Plikus, M. V. et al. Fibroblasts: Origins, definitions, and functions in health and disease. *Cell* **184**, 3852–3872 (2021).
22. Rheinwald, J. G. & Green, H. Serial cultivation of strains of human epidermal keratinocytes: the formation of keratinizing colonies from single cells. *Cell* **6**, 331–343 (1975).
23. Tabula Muris, C. et al. Single-cell transcriptomics of 20 mouse organs creates a Tabula Muris. *Nature* **562**, 367–372 (2018).
24. Joost, S. et al. The molecular anatomy of mouseskin during hair growth and rest. *Cell Stem Cell* **26**, 441–457.e447 (2020).
25. Liu, Y. et al. Single-cell profiling reveals divergent, globally patterned immune responses in murine skin inflammation. *iScience* **23**, 101582 (2020).
26. Ganier, C., Rognoni, E., Goss, G., Lynch, M. & Watt, F. M. Fibroblast heterogeneity in healthy and wounded skin. *Cold Spring Harb. Perspect. Biol.* **14**, https://doi.org/10.1101/cshperspect.a041238 (2022).
27. Driskell, R. R. & Watt, F. M. Understanding fibroblast heterogeneity in the skin. *Trends Cell Biol.* **25**, 92–99 (2015).
28. Phan, Q. M. et al. Lef1 expression in fibroblasts maintains developmental potential in adult skin to regenerate wounds. *Elife* **9**,https://doi.org/10.7554/eLife.60066 (2020).
29. Sola, P. et al. Targeting lymphoid-derived IL-17 signaling to delay skin aging. *Nat. Aging* **3**, 688–704 (2023).
30. Salzer, M. C. et al. Identity noise and adipogenic traits characterize dermal fibroblast aging. *Cell* **175**, 1575–1590.e1522 (2018).
31. Phan, Q. M., Sinha, S., Biernaskie, J. & Driskell, R. R. Single-cell transcriptomic analysis of small and large wounds reveals the distinct spatial organization of regenerative fibroblasts. *Exp. Dermatol.* **30**, 92–101 (2021).
32. Sennett, R. et al. An integrated transcriptome atlas of embryonic hair follicle progenitors, their niche, and the developing skin. *Dev. Cell* **34**, 577–591 (2015).
33. Collins, C. A., Kretzschmar, K. & Watt, F. M. Reprogramming adult dermis to a neonatal state through epidermal activation of beta-catenin. *Development* **138**, 5189–5199 (2011).
34. Mittal, R. et al. Intricate Functions of Matrix Metalloproteinases in Physiological and Pathological Conditions. *J. Cell Physiol.* **231**, 2599–2621 (2016).

35. de Castro Bras, L. E. & Frangogiannis, N. G. Extracellular matrix-derived peptides in tissue remodeling and fibrosis. *Matrix Biol.* **91-92**, 176–187 (2020).
36. Horsnell, H. L. et al. Lymph node homeostasis and adaptation to immune challenge resolved by fibroblast network mechanics. *Nat. Immunol.* **23**, 1169–1182 (2022).
37. Makris, S. et al. Lymph node fibroblast phenotypes and immune crosstalk regulated by podoplanin activity. *Cell Rep.* **44**, 115908 (2025).
38. Midwood, K. S., Chiquet, M., Tucker, R. P. & Orend, G. Tenascin-C at a glance. *J. Cell Sci.* **129**, 4321–4327 (2016).
39. Asai, J. The role of podoplanin in skin diseases. *Int. J. Mol. Sci.* **23**,https://doi.org/10.3390/ijms23031310 (2022).
40. Correa-Gallegos, D. et al. CD201(+) fascia progenitors choreograph injury repair. *Nature* **623**, 792–802 (2023).
41. Jiang, D. et al. Injury triggers fascia fibroblast collective cell migration to drive scar formation through N-cadherin. *Nat. Commun.* **11**, 5653 (2020).
42. Jiang, D. et al. Two succeeding fibroblastic lineages drive dermal development and the transition from regeneration to scarring. *Nat. Cell Biol.* **20**, 422–431 (2018).
43. Driskell, R. R. et al. Distinct fibroblast lineages determine dermal architecture in skin development and repair. *Nature* **504**, 277–281 (2013).
44. Marsh, E., Gonzalez, D. G., Lathrop, E. A., Boucher, J. & Greco, V. Positional stability and membrane occupancy define skin fibroblast homeostasis in vivo. *Cell* **175**, 1620–1633 (2018).
45. Panciera, T., Azzolin, L., Cordenonsi, M. & Piccolo, S. Mechanobiology of YAP and TAZ in physiology and disease. *Nat. Rev. Mol. Cell Biol.* **18**, 758–770 (2017).
46. Rognoni, E. et al. Fibroblast state switching orchestrates dermal maturation and wound healing. *Mol. Syst. Biol.* **14**, e8174 (2018).
47. Lichtenberger, B. M., Mastrogiannaki, M. & Watt, F. M. Epidermal beta-catenin activation remodels the dermis via paracrine signalling to distinct fibroblast lineages. *Nat. Commun.* **7**, 10537 (2016).
48. Jacob, T. et al. Molecular and spatial landmarks of early mouse skin development. *Dev. Cell* **58**, 2140–2162 (2023).
49. Phan, Q. M. et al. Lineage commitment of dermal fibroblast progenitors is controlled by Kdm6b-mediated chromatin demethylation. *EMBO J.* **42**, e113880 (2023).
50. Sorrell, J. M., Baber, M. A. & Caplan, A. I. Site-matched papillary and reticular human dermal fibroblasts differ in their release of specific growth factors/cytokines and in their interaction with keratinocytes. *J. Cell Physiol.* **200**, 134–145 (2004).
51. Wang, Z., Wang, Y., Farhangfar, F., Zimmer, M. & Zhang, Y. Enhanced keratinocyte proliferation and migration in co-culture with fibroblasts. *PLoS ONE* **7**, e40951 (2012).
52. Gallico, G. G. et al. Permanent coverage of large burn wounds with autologous cultured human epithelium. *N. Engl. J. Med.* **311**, 448–451 (1984).
53. Rama, P. et al. Limbal stem-cell therapy and long-term corneal regeneration. *N. Engl. J. Med.* **363**, 147–155 (2010).
54. Hirsch, T. et al. Regeneration of the entire human epidermis using transgenic stem cells. *Nature* **551**, 327–332 (2017).
55. De Rosa, L. et al. Hologene 5: A phase II/III clinical trial of combined cell and gene therapy of junctional epidermolysis bullosa. *Front. Genet.* **12**, 705019 (2021).
56. Enzo, E. et al. Single-keratinocyte transcriptomic analyses identify different clonal types and proliferative potential mediated by FOXM1 in human epidermal stem cells. *Nat. Commun.* **12**, 2505 (2021).
57. Thompson, S. M., Phan, Q. M., Winuthayanon, S., Driskell, I. M. & Driskell, R. R. Parallel single-cell multiomics analysis of neonatal skin reveals the transitional fibroblast states that restrict differentiation into distinct fates. *J. Invest. Dermatol.* **142**, 1812–1823 (2022).
58. Jiang, D. & Rinkevich, Y. Distinct fibroblasts in scars and regeneration. *Curr. Opin. Genet. Dev.* **70**, 7–14 (2021).
59. Korosec, A. et al. Lineage Identity and Location within the Dermis Determine the Function of Papillary and Reticular Fibroblasts in Human Skin. *J. Invest. Dermatol.* **139**, 342–351 (2019).
60. Ascension, A. M., Fuertes-Alvarez, S., Ibanez-Sole, O., Izeta, A. & Arauzo-Bravo, M. J. Human dermal fibroblast subpopulations are conserved across single-cell RNA sequencing studies. *J. Invest. Dermatol.* **141**, 1735–1744.e1735 (2021).
61. Philippeos, C. et al. Spatial and single-cell transcriptional profiling identifies functionally distinct human dermal fibroblast subpopulations. *J. Invest. Dermatol.* **138**, 811–825 (2018).
62. Steele, L. et al. A single-cell and spatial genomics atlas of human skin fibroblasts reveals shared disease-related fibroblast subtypes across tissues. *Nat. Immunol.* **26**, 1807–1820 (2025).
63. Guerrero-Juarez, C. F. et al. Single-cell analysis reveals fibroblast heterogeneity and myeloid-derived adipocyte progenitors in murine skin wounds. *Nat. Commun.* **10**, 650 (2019).
64. Mascharak, S. et al. Preventing engrailed-1 activation in fibroblasts yields wound regeneration without scarring. *Science* **372**,https://doi.org/10.1126/science.aba2374 (2021).
65. Rinkevich, Y. et al. Skin fibrosis. Identification and isolation of a dermal lineage with intrinsic fibrogenic potential. *Science* **348**, aaa2151 (2015).
66. Forsthuber, A. et al. Cancer-associated fibroblast subtypes modulate the tumor-immune microenvironment and are associated with skin cancer malignancy. *Nat. Commun.* **15**, 9678 (2024).
67. Rognoni, E. et al. Role of distinct fibroblast lineages and immune cells in dermal repair following UV radiation-induced tissue damage. *Elife* **10**,https://doi.org/10.7554/eLife.71052 (2021).
68. Thrane, K. et al. Single-cell and spatial transcriptomic analysis of human skin delineates intercellular communication and pathogenic cells. *J. Invest. Dermatol.* **143**, 2177–2192 (2023).
69. Griffin, M. F. et al. Piezo inhibition prevents and rescues scarring by targeting the adipocyte to fibroblast transition. Preprint at https://doi.org/10.1101/2023.04.03.535302 (2023).
70. Talbott, H. E., Mascharak, S., Griffin, M., Wan, D. C. & Longaker, M. T. Wound healing, fibroblast heterogeneity, and fibrosis. *Cell Stem Cell* **29**, 1161–1180 (2022).
71. Andersen, M. S. et al. Tracing the cellular dynamics of sebaceous gland development in normal and perturbed states. *Nat. Cell Biol.* **21**, 924–932 (2019).
72. Bansaccal, N. et al. The extracellular matrix dictates regional competence for tumour initiation. *Nature* **623**, 828–835 (2023).
73. Tanimura, S. et al. Hair follicle stem cells provide a functional niche for melanocyte stem cells. *Cell Stem Cell* **8**, 177–187 (2011).
74. Greco, V. et al. A two-step mechanism for stem cell activation during hair regeneration. *Cell Stem Cell* **4**, 155–169 (2009).
75. Rezza, A. et al. Signaling networks among stem cell precursors, transit-amplifying progenitors, and their niche in developing hair follicles. *Cell Rep.* **14**, 3001–3018 (2016).
76. Chen, D. et al. Fibroblast bioelectric signaling drives hair growth. *Cell* **188**, 5175–5193 (2025).
77. Shook, B. A. et al. Myofibroblast proliferation and heterogeneity are supported by macrophages during skin repair. *Science* **362**,https://doi.org/10.1126/science.aar2971 (2018).
78. Cai, X. et al. Tenascin C(+) papillary fibroblasts facilitate neuroimmune interaction in a mouse model of psoriasis. *Nat. Commun.* **14**, 2004 (2023).
79. Xu, Z. et al. Anatomically distinct fibroblast subsets determine skin autoimmune patterns. *Nature* **601**, 118–124 (2022).
80. Kyprianou, C. et al. Basement membrane remodelling regulates mouse embryogenesis. *Nature* **582**, 253–258 (2020).

81. Trappmann, B. et al. Extracellular-matrix tethering regulates stem-cell fate. *Nat. Mater.* **11**, 642–649 (2012).
82. Zijl, S. et al. Micro-scaled topographies direct differentiation of human epidermal stem cells. *Acta Biomater.* **84**, 133–145 (2019).
83. Roig-Rosello, E. et al. Dermal stiffness governs the topography of the epidermis and the underlying basement membrane in young and old human skin. *Aging Cell* **23**, e14096 (2024).
84. Chung, M. I., Bujnis, M., Barkauskas, C. E., Kobayashi, Y. & Hogan, B. L. M. Niche-mediated BMP/SMAD signaling regulates lung alveolar stem cell proliferation and differentiation. *Development* **145**,https://doi.org/10.1242/dev.163014 (2018).
85. Snippert, H. J. et al. Intestinal crypt homeostasis results from neutral competition between symmetrically dividing Lgr5 stem cells. *Cell* **143**, 134–144 (2010).
86. Muzumdar, M. D., Tasic, B., Miyamichi, K., Li, L. & Luo, L. A global double-fluorescent Cre reporter mouse. *Genesis* **45**, 593–605 (2007).
87. Maciag, G. et al. JAK/STAT signaling promotes the emergence of unique cell states in ulcerative colitis. *Stem Cell Rep.* **19**, 1172–1188 (2024).
88. Stoeckius, M. et al. Cell Hashing with barcoded antibodies enables multiplexing and doublet detection for single cell genomics. *Genome Biol.* **19**, 224 (2018).
89. Wolf, F. A., Angerer, P. & Theis, F. J. SCANPY: large-scale single-cell gene expression data analysis. *Genome Biol.* **19**, 15 (2018).
90. Hao, Y. et al. Integrated analysis of multimodal single-cell data. *Cell* **184**, 3573–3587 (2021).
91. Germain, P. L., Lun, A., Garcia Meixide, C., Macnair, W. & Robinson, M. D. Doublet identification in single-cell sequencing data using scDblFinder. *F1000Res.* **10**, 979 (2021).
92. Korsunsky, I. et al. Fast, sensitive and accurate integration of single-cell data with Harmony. *Nat. Methods* **16**, 1289–1296 (2019).
93. Finak, G. et al. MAST: a flexible statistical framework for assessing transcriptional changes and characterizing heterogeneity in single-cell RNA sequencing data. *Genome Biol.* **16**, 278 (2015).
94. Jin, S., Plikus, M. V. & Nie, Q. CellChat for systematic analysis of cell-cell communication from single-cell transcriptomics. *Nat. Protoc.* **20**, 180–219 (2025).
95. Ergen, C. et al. Consensus prediction of cell type labels in single-cell data with popV. *Nat. Genet.* **56**, 2731–2738 (2024).
96. Gayoso, A. et al. A Python library for probabilistic analysis of single-cell omics data. *Nat. Biotechnol.* **40**, 163–166 (2022).
97. Hie, B., Bryson, B. & Berger, B. Efficient integration of heterogeneous single-cell transcriptomes using Scanorama. *Nat. Biotechnol.* **37**, 685–691 (2019).
98. Biancalani, T. et al. Deep learning and alignment of spatially resolved single-cell transcriptomes with Tangram. *Nat. Methods* **18**, 1352–1362 (2021).
99. Rahimi, A., Vale-Silva, L. A., Falth Savitski, M., Tanevski, J. & Saez-Rodriguez, J. DOT: a flexible multi-objective optimization framework for transferring features across single-cell and spatial omics. *Nat. Commun.* **15**, 4994 (2024).
100. Virtanen, P. et al. SciPy 1.0: fundamental algorithms for scientific computing in Python. *Nat. Methods* **17**, 261–272 (2020).
101. Liao, Y., Smyth, G. K. & Shi, W. The R package Rsubread is easier, faster, cheaper and better for alignment and quantification of RNA sequencing reads. *Nucleic Acids Res.* **47**, e47 (2019).
102. Robinson, M. D., McCarthy, D. J. & Smyth, G. K. edgeR: a Bioconductor package for differential expression analysis of digital gene expression data. *Bioinformatics* **26**, 139–140 (2010).
103. Love, M. I., Huber, W. & Anders, S. Moderated estimation of fold change and dispersion for RNA-seq data with DESeq2. *Genome Biol.* **15**, 550 (2014).
104. Subramanian, A. et al. Gene set enrichment analysis: a knowledge-based approach for interpreting genome-wide expression profiles. *Proc. Natl. Acad. Sci. USA* **102**, 15545–15550 (2005).
105. Castanza, A. S. et al. Extending support for mouse data in the Molecular Signatures Database (MSigDB). *Nat. Methods* **20**, 1619–1620 (2023).
106. Gu, Z., Eils, R. & Schlesner, M. Complex heatmaps reveal patterns and correlations in multidimensional genomic data. *Bioinformatics* **32**, 2847–2849 (2016).
107. Livak, K. J. & Schmittgen, T. D. Analysis of relative gene expression data using real-time quantitative PCR and the 2(-Delta Delta C(T)) Method. *Methods* **25**, 402–408 (2001).
108. Bankhead, P. et al. QuPath: Open source software for digital pathology image analysis. *Sci. Rep.* **7**, 16878 (2017).
109. Dobin, A. et al. STAR: ultrafast universal RNA-seq aligner. *Bioinformatics* **29**, 15–21 (2013).
110. Xu, S. et al. Using clusterProfiler to characterize multiomics data. *Nat. Protoc.* **19**, 3292–3320 (2024).
111. Almeida-Marques, C. et al. Secretome processing for proteomics: A methods comparison. *Proteomics* **24**, e2300262 (2024).
112. Polito, M. P. et al. Biochemical characterization of the feedforward loop between CDK1 and FOXM1 in epidermal stem cells. *Biol. Direct* **19**, 91 (2024).
113. Scalvini, L. et al. Identification of pyrazolo-piperidinone derivatives targeting YAP-TEAD interface 3 as anticancer agents through integrated virtual screening and mass spectrometry proteomics. *Eur. J. Med. Chem.* **300**, 118056 (2025).
114. Santos, A. et al. A knowledge graph to interpret clinical proteomics data. *Nat. Biotechnol.* **40**, 692–702 (2022).
115. Lazar, C., Gatto, L., Ferro, M., Bruley, C. & Burger, T. Accounting for the Multiple Natures of Missing Values in Label-Free Quantitative Proteomics Data Sets to Compare Imputation Strategies. *J. Proteome Res.* **15**, 1116–1125 (2016).
116. UniProt, C. UniProt: the Universal Protein Knowledgebase in 2023. *Nucleic Acids Res.* **51**, D523–D531 (2023).
117. Mellacheruvu, D. et al. The CRAPome: a contaminant repository for affinity purification-mass spectrometry data. *Nat. Methods* **10**, 730–736 (2013).
118. Szklarczyk, D. et al. The STRING database in 2021: customizable protein-protein networks, and functional characterization of user-uploaded gene/measurement sets. *Nucleic Acids Res.* **49**, D605–D612 (2021).
119. van Dongen, S. & Abreu-Goodger, C. Using MCL to extract clusters from networks. *Methods Mol. Biol.* **804**, 281–295 (2012).
120. Butt, H. J. & Jaschke, M. Calculation of Thermal Noise in Atomic-Force Microscopy. *Nanotechnology* **6**, 1–7 (1995).
121. Kontomaris, S. V., Malamou, A. & Stylianou, A. The Hertzian theory in AFM nanoindentation experiments regarding biological samples: Overcoming limitations in data processing. *Micron***155**, https://doi.org/10.1016/j.micron.2022.103228 (2022).

Acknowledgements

We thank J. Martin Gonzalez and the Core Facility for Transgenic Mice for mice rederivation and support; the staff of the animal facility (AEM); K.B. Jensen for mice; A. Kalvisa, H. Wollmann, M. Michaut, and the reNEW Genomics Platform for support, technical expertise, and use of instruments; G. Dela Cruz, M. Maimets, and P. van Dieken, and the reNEW Flow Cytometry Platform for support, technical expertise, and use of instruments; J. Bulkescher, J. Viswalingam Bagge and A. Georgantzoglou and the reNEW Microscopy Facility for the help with microscopy and image analysis; D. Andrejeva and the Centre for Health Data Science for assistance with bulk RNA-seq analysis; T. Voet, K. Vandereyken, N. Vandermeulen and the KU Leuven Institute for Single Cell Omics (LISCO) for the performance of the 10x Genomics Xenium assays. We

thank the staff members of the Proteomics Research Infrastructure (PRI) for mass spectrometry based proteomic analysis and data analysis, performed at the University of Copenhagen (UCPH), supported by the Novo Nordisk Foundation (NNF) (grant agreement number NNF19SA0059305). We also thank Prof. Michele De Luca (UNIMORE) for providing the 3T3-J2 cells and Prof. Graziella Pellegrini (UNIMORE) for providing human primary epidermal keratinocytes. We are grateful to all the other members of the Aragona lab for fruitful discussions and members of reNEW for constant feedback.

Author contributions

C.A.S and M.A. designed the experiments and performed data analysis; C.A.S. performed most of the experiments; L.B. helped with experiments; I.K. helped with mice; C.A.S. performed bioinformatic analysis of the bulk RNA-seq data; C.A. and A.S. performed all single-cell and spatial transcriptomics bioinformatic analyses. G.A.G., M.P.P., G.B., and E.E. performed human in vitro experiments. L.T. and M.P.C. performed secretome analysis, A.A. performed AFM analysis. C.A.S, C.A., and M.A. wrote the manuscript with comments and suggestions from E.E. and A.S. M.A. supervised the work.

Funding

Work in the Aragona Lab was funded by the Leo Foundation Research Grant (LC-OC-23001145), the Independent Research Fund Denmark (DFF) (1030-00100B) and the Novo Nordisk Foundation (NNF20OC0064992). C.A.S was supported by the NNF Copenhagen Bioscience PhD programme (NNF20SA0035584). In addition, the work was funded by Leuven Future Fund (LISCO-BIOMED), Opening the Future Fund, and KU Leuven ID-N (3E210655 COLUMBO) in the AS lab; Project 2022KRTKXS (CUP E53D23007430006) in the EE lab, and Project 2022WYAZ47 (CUP E53D23009570006) in the MPC lab, both within the National Recovery and Resilience Plan (NRRP), Mission 4, Component 2 Investment 1.1 for the National Research Programme (PNR) and Research Projects of Significant National Interest (PRIN)", funded by the European Union – NextGenerationEU - ref. D.D. No.104 of 02/02/2022. GAG is recipient of a PhD fellowship funded by European Union – NextGenerationEU – Mission 4, Component 2, CUP E93C22001080001, within the framework of the "National Centre for Gene Therapy and Drugs based on RNA Technology" (National Research Centre for the Development of Gene Therapy and RNA-based Drugs), project code CN00000041 – National Recovery and Resilience Plan (PNRR) – Mission 4 "Education and Research", Component 2 "From research to business", Investment 1.4 "Strengthening research facilities and creation of 'national R&D champions' in selected Key Enabling Technologies", ref. MUR Call 3138/2021 as amended by DD 3175/2021. The Novo Nordisk Foundation Centre for Stem Cell Medicine is supported by the Novo Nordisk Foundation (NNF21CC0073729).

Competing interests

The authors declare no competing financial and non-financial interests.

Additional information

Supplementary information The online version contains supplementary material available at https://doi.org/10.1038/s41467-026-73979-0.

Correspondence and requests for materials should be addressed to Elena Enzo, Alejandro Sifrim or Mariaceleste Aragona.

Peer review information *Nature Communications* thanks the anonymous reviewer(s) for their contribution to the peer review of this work. A peer review file is available.